A GENERALIZED COSSERAT POINT ELEMENT (CPE) FOR ISOTROPIC NONLINEAR ELASTIC MATERIALS INCLUDING IRREGULAR 3-D BRICK AND THIN STRUCTURES

M. Jabareen and M. B. Rubin

A GENERALIZED COSSERAT POINT ELEMENT (CPE) FOR ISOTROPIC NONLINEAR ELASTIC MATERIALS INCLUDING IRREGULAR 3-D BRICK AND THIN STRUCTURES

M. Jabareen and M. B. Rubin

A generalized form for the strain energy of inhomogeneous deformations is developed for a 3-D brick Cosserat Point Element (CPE) which includes full coupling of bending and torsional modes of deformation. The constitutive coefficients, which depend on the reference geometry of the element, are determined by solving eighteen bending problems and six torsion problems on special elements that are parallelepipeds with two right angles. The resulting constitutive coefficients ensure that the strain energy for inhomogeneous deformations remains a positive definite function of the inhomogeneous strain measures for all reference element shapes. A number of example problems are considered which show that the generalized CPE produces results as accurate as enhanced strain and incompatible elements for thin structures and is free of hourglass instabilities typically predicted by these enhanced elements in regions experiencing combined high compression with bending.

1. Introduction

Recently, Nadler and Rubin [2003] developed a 3-D eight noded brick element based on the theory of a Cosserat point [Rubin 1995; 2000]. This Cosserat point element (CPE) can be used to formulate the numerical solution of dynamic problems for nonlinear hyperelastic materials. The kinematics of the CPE are characterized by eight element director vectors and the kinetics propose eight balance laws of director momentum to determine the dynamic response of the element. The locations of the nodes in the current deformed configuration are characterized by eight nodal director vectors and the element directors are related to the nodal directors by standard tri-linear shape functions. Moreover, the CPE theory considers the element as a structure and introduces a strain energy function which characterizes the response of the structure. Also, the nodal forces are related to derivatives of the strain energy function through algebraic relations in a similar manner to the relationship of the stress to derivatives of the strain energy function in the full three-dimensional theory of hyperelastic materials.

The CPE can easily be implemented into standard finite element programs. Specifically, the nodal positions (nodal director vectors) are used as input variables to determine the nodal forces and tangent stiffness as output variables. Here, the element assembly and solution procedures in the computer program FEAP [Taylor 2005] were used to satisfy the equilibrium equations by updating the present nodal director vectors.

In the standard finite element procedures for hyperelastic materials the response of the element is determined by integrals over the element region which assume that the kinematic approximation is valid pointwise. This is in contrast with the CPE which needs no integration over the element region. In

this regard, the nodal forces in the CPE are not determined by integration of a displacement field based on shape functions. However, the CPE approach does not use a mixed approach based on separate shape functions for kinematic and kinetic quantities. Specifically, the nodal forces are determined by the nodal directors through algebraic constitutive equations characterizing the structural response of the element. Furthermore, it is known [Zienkiewicz and Taylor 2005] that the standard element based on full integration is robust but that it exhibits unphysical locking for thin structures with poor element aspect ratios and for nearly incompressible materials. Special methods based on enhanced strains, incompatible modes and reduced integration with hourglass control have been developed to overcome these problems; see, e.g., [Belytschko et al. 1984; Simo and Rifai 1990; Simo and Armero 1992; Belytschko and Binde-man 1993; Simo et al. 1993; Bonet and Bhargava 1995; Reese and Wriggers 1996; 2000; Reese et al. 2000; Hutter et al. 2000]. However, these improved formulations can exhibit unphysical hourglassing in regions experiencing combined high compression with bending; see, for example, [Reese and Wriggers 1996; 2000; Loehnert et al. 2005; Jabareen and Rubin 2007a; 2008c]. Furthermore, it was shown in [Jabareen and Rubin 2007a] that some of these improved element formulations in commercial codes can exhibit inelastic response even though they attempt to model a hyperelastic material with a strain energy function.

Restrictions were developed on the strain energy function for the CPE which ensure that the element reproduces exact solutions for all homogeneous deformations [Nadler and Rubin 2003]. Consequently, the CPE automatically satisfies a nonlinear form of the patch test. Also, a functional form of the strain energy for the CPE was proposed with specific dependence on the strain energy of the three-dimensional material and the reference geometry of the CPE element. In addition, a strain energy function for inho-mogeneous deformations was introduced as a quadratic function of inhomogeneous strain measures.

In the original CPE formulation [Nadler and Rubin 2003] the coefficients in the strain energy func-tion for inhomogeneous deformations where determined by comparing linear solutions of a rectangular parallelepiped CPE with exact solutions of the linear three-dimensional equations for pure bending, pure torsion and higher-order hourglass modes of deformation. Loehnert et al. [2005] implemented the CPE formulation into the finite element code FEAP [Taylor 2005] and considered specific example problems which showed that the response of the original CPE was robust and locking free for thin structures. However, it was also shown that the accuracy of the original CPE degraded with increased irregularity of the reference element shape.

Recently, Boerner et al. [2007] have proposed a numerical method for determining coefficients in a quadratic form of the strain energy function for inhomogeneous deformations which improve the response of the CPE for 2-D plane strain problems with irregular elements. In [Jabareen and Rubin 2007b] analyt-ical expressions were developed for constitutive coefficients in an improved CPE for 3-D deformations by generalizing the quadratic form of the strain energy function for inhomogeneous deformations to include additional coupling of the inhomogeneous strains active in bending modes. Functional forms for the additional coefficients were determined by considering four bending solutions for special shaped reference elements which are parallelepipeds with two right angles. In [Jabareen and Rubin 2008c] improved coefficients were developed for torsion by considering an exact torsion-like solution of the linear elastic equations for an isotropic elastic material.

In this paper, exact linear solutions of bending and simple torsion of these special elements are re-examined and it is shown that by including more general coupling of bending and torsional modes it

is possible to match solutions of the two additional bending modes not handled in [Jabareen and Rubin 2007b] as well as the simple torsion solutions. Matching these additional two bending modes significantly improves the response of the generalized CPE for the problem of bending of a thin rhombic plate, which was shown to be inaccurate in [Ehrlich 2007].

Here is an outline of this paper. Section 2 presents the basic equations of the CPE. Section 3 describes the procedure to use eighteen bending solutions and six torsions solutions to determine the functional forms of the constitutive coefficients in the strain energy function for inhomogeneous deformations. Section 4 considers a number of examples that demonstrate the response of the generalized CPE. Finally, Section 5 presents conclusions.
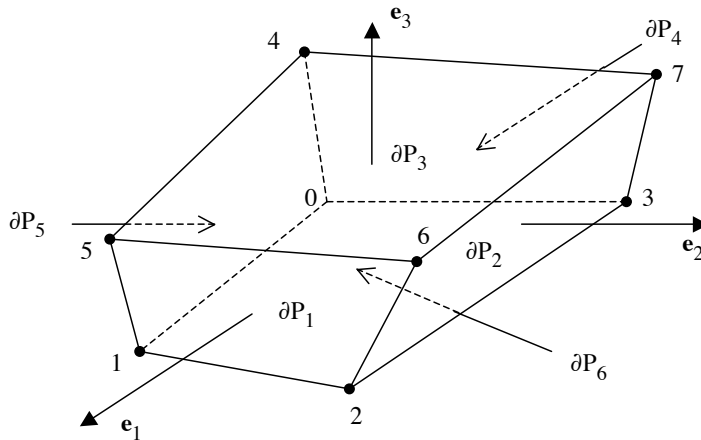
2. Basic equations of a Cosserat point element (CPE)

Here attention is focused on an eight noded 3-D brick CPE as developed in [Nadler and Rubin 2003] and modified in [Jabareen and Rubin 2008c; Jabareen and Rubin 2007b]. Moreover, for the present discussion it is sufficient to confine attention to the equilibrium equations. Within the context of this theory the kinematics of the CPE are characterized by

$$\{\boldsymbol{D}_i, \boldsymbol{d}_i\} \quad (i = 0, 1, 2 \ldots, 7), \tag{2.1}$$

where $\boldsymbol{D}_i$ are constant reference directors associated with the reference configuration and $\boldsymbol{d}_i$ are present directors associated with the deformed present configuration. These element director vectors are related to the nodal director vectors [which locate the nodes of a brick element (see Figure 1) relative to a fixed origin] by a constant matrix and details can be found in [Nadler and Rubin 2003].

Without loss in generality, the three-dimensional position vector $\boldsymbol{X}^*$ associated with material points in the reference configuration of the element can be expressed in the form

$$\boldsymbol{X}^*(\theta^1, \theta^2, \theta^3) = \sum_{j=0}^{7} N^j(\theta^1, \theta^2, \theta^3) \boldsymbol{D}_j, \qquad |\theta^1| \le \frac{H_1}{2}, \quad |\theta^2| \le \frac{H_2}{2}, \quad |\theta^3| \le \frac{H_3}{2}, \tag{2.2}$$

Figure 1. Sketch of a general brick CPE showing the numbering of the nodes and the surfaces.

where θ^i $(i = 1, 2, 3)$ are convected material coordinates having the units of lengths, H_i are constant lengths characterizing the element defined by

$$|\boldsymbol{D}_1| = 1, \qquad |\boldsymbol{D}_2| = 1, \qquad |\boldsymbol{D}_3| = 1, \tag{2.3}$$

and N^i are shape functions

$$N^0 = 1, \quad N^1 = \theta^1, \quad N^2 = \theta^2, \quad N^3 = \theta^3, \quad N^4 = \theta^1\theta^2, \quad N^5 = \theta^1\theta^3, \quad N^6 = \theta^2\theta^3, \quad N^7 = \theta^1\theta^2\theta^3. \tag{2.4}$$

Moreover, the region P_0 associated with the reference configuration is mapped to the region P associated with the present configuration, which is bounded by ∂P which is characterized by the six surfaces ∂P_J $(J = 1, 2, \ldots, 6)$, such that

$$\partial P = \partial P_1 \cup \partial P_2 \cup \partial P_3 \cup \partial P_4 \cup \partial P_5 \cup \partial P_6,$$

$$\theta^1 = +\frac{H_1}{2} \quad \text{on } \partial P_1, \qquad \theta^2 = +\frac{H_2}{2} \quad \text{on } \partial P_2, \qquad \theta^3 = +\frac{H_3}{2} \quad \text{on } \partial P_3,$$

$$\theta^1 = -\frac{H_1}{2} \quad \text{on } \partial P_4, \qquad \theta^2 = -\frac{H_2}{2} \quad \text{on } \partial P_5, \qquad \theta^3 = -\frac{H_3}{2} \quad \text{on } \partial P_6. \tag{2.5}$$

The element directors and nodal directors are related using a tri-linear form like (2.2) for the position vector $\boldsymbol{x}^*$ of material points in the present configuration. This causes the displacement field to be continuous across element boundaries. However, it is important to emphasize that the constitutive equations in the CPE approach are determined by a strain energy function for the structure and do not depend on the pointwise validity of this approximate expression for $\boldsymbol{x}^*$.

Now, in the absence of body force, the equilibrium forms of the balances of director momentum become

$$\boldsymbol{m}^i = \boldsymbol{t}^i \quad \text{with } (\boldsymbol{t}^0 = 0) \text{ and } (i = 0, 1, 2, \ldots, 7), \tag{2.6}$$

where $\boldsymbol{m}^i$ are director couples due to surface tractions on the boundaries of the element, and $\boldsymbol{t}^i$ are intrinsic director couples which require constitutive equations. In this regard, it is mentioned that director couples are kinetic quantities conjugate to the element directors and they do not necessarily have the units of mechanical moment.

For the CPE it is convenient to introduce the deformation measures

$$\boldsymbol{F} = \sum_{i=1}^{3} \boldsymbol{d}_i \otimes \boldsymbol{D}^i, \qquad \boldsymbol{\beta}_i = \boldsymbol{F}^{-1}\boldsymbol{d}_{i+3} - \boldsymbol{D}_{i+3} \ (i = 1, 2, 3, 4), \qquad \bar{\boldsymbol{F}} = \boldsymbol{F}\left(\boldsymbol{I} + \sum_{i=1}^{4} \boldsymbol{\beta}_i \otimes \boldsymbol{V}^i\right), \tag{2.7}$$

where $\{\boldsymbol{D}^i, \boldsymbol{d}^i\}$ $(i = 1, 2, 3)$ are the reciprocal vectors of $\{\boldsymbol{D}_i, \boldsymbol{d}_i\}$, respectively, and $\{V, \boldsymbol{V}^i\}$ characterize the reference configuration of the element and are defined in [Nadler and Rubin 2003, Appendix B]. Specifically, when the reference CPE is a rectangular parallelepiped then V represents the volume of the CPE and $\boldsymbol{V}^i$ vanish. Nadler and Rubin [2003] developed restrictions on the strain energy of an elastic CPE which ensure that the element satisfies a nonlinear form of the patch test for all uniform homogeneous nonlinear elastic anisotropic materials. In particular, the specific (per unit mass) strain energy Σ of the CPE can be expressed in terms of the specific strain energy Σ^* of the three-dimensional material and the specific strain energy Ψ associated with inhomogeneous deformations, such that

$$\Sigma = \Sigma^*(\bar{\boldsymbol{C}}) + \Psi(\bar{\boldsymbol{C}}, \kappa_j^i), \tag{2.8}$$

where the kinematic quantities $\{\bar{C}, \kappa_j^i\}$ are defined by

$$\bar{C} = \bar{F}^T \bar{F},$$

$$\kappa_1^1 = H_2 \boldsymbol{\beta}_1 \cdot \boldsymbol{D}^1, \qquad \kappa_1^2 = H_1 \boldsymbol{\beta}_1 \cdot \boldsymbol{D}^2, \qquad \kappa_1^3 = H_3 \boldsymbol{\beta}_1 \cdot \boldsymbol{D}^3,$$

$$\kappa_2^1 = H_3 \boldsymbol{\beta}_2 \cdot \boldsymbol{D}^1, \qquad \kappa_2^2 = H_2 \boldsymbol{\beta}_2 \cdot \boldsymbol{D}^2, \qquad \kappa_2^3 = H_1 \boldsymbol{\beta}_2 \cdot \boldsymbol{D}^3,$$

$$\kappa_3^1 = H_1 \boldsymbol{\beta}_3 \cdot \boldsymbol{D}^1, \qquad \kappa_3^2 = H_3 \boldsymbol{\beta}_3 \cdot \boldsymbol{D}^2, \qquad \kappa_3^3 = H_2 \boldsymbol{\beta}_3 \cdot \boldsymbol{D}^3,$$

$$\kappa_4^1 = H_2 H_3 \boldsymbol{\beta}_4 \cdot \boldsymbol{D}^1, \quad \kappa_4^2 = H_1 H_3 \boldsymbol{\beta}_4 \cdot \boldsymbol{D}^2, \quad \kappa_4^3 = H_1 H_2 \boldsymbol{\beta}_4 \cdot \boldsymbol{D}^3. \tag{2.9}$$

Here, it is convenient to introduce the alternative variables b_i ($i = 1, 2, \ldots, 12$) by

$$b_i = \{\kappa_1^1, \kappa_3^3, \kappa_1^2, \kappa_2^3, \kappa_2^1, \kappa_3^2, \kappa_1^3, \kappa_2^2, \kappa_3^1, \kappa_4^1, \kappa_4^2, \kappa_4^3\}. \tag{2.10}$$

Then, following [Jabareen and Rubin 2008c; Jabareen and Rubin 2007b], the strain energy Ψ for inhomogeneous deformations is expressed in the form

$$2m\Psi = \frac{D^{1/2} V \mu}{6(1 - \nu)} \left(\sum_{i=1}^{12} \sum_{j=1}^{12} B_{ij} b_i b_j \right), \tag{2.11}$$

where m is the mass of the element, $\{\mu, \nu\}$ are the shear modulus and Poisson's ratio associated with the small deformation response, B_{ij} is a constant symmetric matrix with the response to higher order hourglassing being uncoupled from that to bending and torsion so that B_{ij} has the following zero components:

$$\begin{aligned} B_{ij} = 0 \quad &\text{for } i = 10 \text{ and } j \neq 10, \\ B_{ij} = 0 \quad &\text{for } i = 11 \text{ and } j \neq 11, \\ B_{ij} = 0 \quad &\text{for } i = 12 \text{ and } j \neq 12, \end{aligned} \tag{2.12}$$

and the values of $\{B_{(10,10)}, B_{(11,11)}, B_{(12,12)}\}$ are given by the expressions associated with higher order hourglassing in [Nadler and Rubin 2003]. It then can be shown (loc. cit.) that the constitutive equations for a hyperelastic CPE become

$$d^{1/2} \boldsymbol{T} = 2m \bar{\boldsymbol{F}} \frac{\partial \Sigma^*(\bar{C})}{\partial \bar{C}} \bar{\boldsymbol{F}}^T,$$

$$\boldsymbol{t}^4 = \left(m \frac{\partial \Psi}{\partial b_1} H_2 \boldsymbol{d}^1 + m \frac{\partial \Psi}{\partial b_3} H_1 \boldsymbol{d}^2 + m \frac{\partial \Psi}{\partial b_7} H_3 \boldsymbol{d}^3 \right) + (d^{1/2} \boldsymbol{T})(\bar{\boldsymbol{F}}^{-T} \boldsymbol{V}^1),$$

$$\boldsymbol{t}^5 = \left(m \frac{\partial \Psi}{\partial b_5} H_3 \boldsymbol{d}^1 + m \frac{\partial \Psi}{\partial b_8} H_2 \boldsymbol{d}^2 + m \frac{\partial \Psi}{\partial b_4} H_1 \boldsymbol{d}^3 \right) + (d^{1/2} \boldsymbol{T})(\bar{\boldsymbol{F}}^{-T} \boldsymbol{V}^2),$$

$$\boldsymbol{t}^6 = \left(m \frac{\partial \Psi}{\partial b_9} H_1 \boldsymbol{d}^1 + m \frac{\partial \Psi}{\partial b_6} H_3 \boldsymbol{d}^2 + m \frac{\partial \Psi}{\partial b_2} H_2 \boldsymbol{d}^3 \right) + (d^{1/2} \boldsymbol{T})(\bar{\boldsymbol{F}}^{-T} \boldsymbol{V}^3),$$

$$\boldsymbol{t}^7 = \left(m \frac{\partial \Psi}{\partial b_{10}} H_2 H_3 \boldsymbol{d}^1 + m \frac{\partial \Psi}{\partial b_{11}} H_1 H_3 \boldsymbol{d}^2 + m \frac{\partial \Psi}{\partial b_{12}} H_1 H_2 \boldsymbol{d}^3 \right), \tag{2.13}$$

and the remaining quantities t^i are determined by

$$t^i = \left(d^{1/2}T - \sum_{j=4}^{7} t^j \otimes d_j\right)\cdot d^i \quad (i = 1, 2, 3).$$ (2.14)

These constitutive equations automatically satisfy a nonlinear form of the patch test [Nadler and Rubin 2003].

Next, for elastically isotropic materials it is convenient to use the work of Flory [1961] to introduce the dilation $\bar{J}$, the pure measures of distortion $\{\bar{F}', \bar{C}'\}$ and the scalar measures of distortion $\{\alpha_1, \alpha_2\}$

$$\bar{J} = \det(\bar{F}), \quad \bar{F}' = \bar{J}^{-1/3}\bar{F}, \quad \bar{C}' = \bar{F}'^T \bar{F}', \quad \alpha_1 = \bar{C}' \cdot I, \quad \alpha_2 = \bar{C}' \cdot \bar{C}'.$$ (2.15)

Then, the strain energy function Σ^* can be written in the form

$$\Sigma^* = \hat{\Sigma}^*(\bar{J}, \alpha_1, \alpha_2),$$ (2.16)

so that

$$\frac{\partial \Sigma^*}{\partial \bar{C}} = \frac{\partial \hat{\Sigma}^*}{\partial \bar{J}}\left(\tfrac{1}{2}\bar{J}\bar{C}^{-1}\right) + \frac{\partial \hat{\Sigma}^*}{\partial \alpha_1}\left(\bar{J}^{-2/3}\left(I - \tfrac{1}{3}(\bar{C}\cdot I)\bar{C}^{-1}\right)\right) + \frac{\partial \hat{\Sigma}^*}{\partial \alpha_2}\left(2\bar{J}^{-4/3}\left(\bar{C} - \tfrac{1}{3}(\bar{C}\cdot\bar{C})\bar{C}^{-1}\right)\right).$$ (2.17)

Also, for the example problems considered later Σ^* is specified in terms of the small deformation bulk modulus K and shear modulus μ, such that

$$\rho_0^* \Sigma^* = \frac{1}{2}K(\bar{J} - 1)^2 + \mu(\alpha_1 - 3),$$ (2.18)

where ρ_0^* is the constant reference density of the material, the mass m of the CPE is given by

$$m = \rho_0^* D^{1/2} V.$$ (2.19)

and K and Young's modulus E associated with the small deformation response satisfy the equations

$$K = \frac{2\mu(1+\nu)}{3(1-2\nu)}, \qquad E = 2\mu(1+\nu).$$ (2.20)

Furthermore, for later reference it can be shown [Nadler and Rubin 2003] that the director couples m^i are related to the traction vector t^* applied to the boundary ∂P by the integrals

$$m^i = \int_{\partial P} N^i t^* da^* \quad (i = 0, 1, \dots, 7),$$ (2.21)

where da^* is the current element of area. Also, it can be shown [Loehnert et al. 2005] that $d^{1/2}T$ is equal to the volume integral of the three-dimensional Cauchy stress T^*

$$d^{1/2}T = \int_P T^* dv^*,$$ (2.22)

where dv^* is the current element of volume.

3. Determination of the constitutive coefficients

In this paper the constitutive coefficients B_{ij} in (2.11) are determined by matching solutions of the linearized equations for the CPE with exact solutions of the linear theory of elasticity for special element shapes. Specifically, the classical pure bending solution (e.g., [Sokolnikoff 1956]) of the three dimensional equations of elasticity for a rectangular parallelepiped can be written in the form

$$X^* = X_i^{*\prime} e_i', \qquad u^* = u_i^{*\prime} e_i', \qquad T^* = T_{ij}^{*\prime}(e_i' \otimes e_j'), \quad (i, j = 1, 2, 3)$$

$$u_1^{*\prime} = \gamma\, X_1^{*\prime} X_2^{*\prime}, \quad u_2^{*\prime} = -\tfrac{1}{2}\gamma\left((X_1^{*\prime})^2 + \nu(X_2^{*\prime})^2 - \nu(X_3^{*\prime})^2\right), \quad u_3^{*\prime} = -\gamma\, \nu X_2^{*\prime} X_3^{*\prime},$$

$$T_{11}^{*\prime} = 2\mu(1 + \nu^*)\gamma\, X_2^{*\prime}, \quad \text{all other } T_{ij}^{*\prime} = 0. \tag{3.1}$$

In this solution, X^* locates a material point in the reference configuration, u^* is the displacement vector, T^* is the stress tensor, the constant γ controls the magnitude of the bending field and the components of the tensors are referred to the right-handed orthonormal base vectors e_i' ($i = 1, 2, 3$). Also, the simple torsion-like solution in [Jabareen and Rubin 2008c] can be expressed in the form

$$u^* = (-\omega\phi X_2^{*\prime} X_3^{*\prime})e_1' + (-\omega X_1^{*\prime} X_3^{*\prime})e_2' + (\omega X_1^{*\prime} X_2^{*\prime})e_3',$$

$$T^* = \mu\omega[-(1 + \phi)X_3^{*\prime}(e_1' \otimes e_2' + e_2' \otimes e_1') + (1 - \phi)X_2^{*\prime}(e_1' \otimes e_3' + e_3' \otimes e_1')], \tag{3.2}$$

where the constant ω is the twist per unit length in the e_1' direction and the constant ϕ controls the warping of the cross-section with unit normal e_1'.

In order to determine values of the coefficients B_{ij} it is convenient to consider the following three elements shapes, which are defined in terms of another fixed rectangular Cartesian triad e_i as follows:

Element E1 ($D_{12} \neq 0$, $D_{13} = 0$, $D_{23} = 0$)

$$D_1 = e_1, \quad D_2 = D_{12}e_1 + \sqrt{1 - D_{12}^2}\,e_2, \quad D_3 = e_3, \quad D_i = 0 \quad (i = 0, 4, 5, 6, 7), \tag{3.3a}$$

Element E2 ($D_{12} = 0$, $D_{13} \neq 0$, $D_{23} = 0$)

$$D_1 = e_1, \quad D_2 = e_2, \quad D_3 = D_{13}e_1 + \sqrt{1 - D_{13}^2}\,e_3, \quad D_i = 0 \quad (i = 0, 4, 5, 6, 7), \tag{3.3b}$$

Element E3 ($D_{12} = 0$, $D_{13} = 0$, $D_{23} \neq 0$)

$$D_1 = e_1, \quad D_2 = e_2, \quad D_3 = D_{23}e_2 + \sqrt{1 - D_{23}^2}\,e_3, \quad D_i = 0 \quad (i = 0, 4, 5, 6, 7), \tag{3.3c}$$

where the metric D_{ij} is defined by

$$D_{ij} = D_i \cdot D_j. \tag{3.4}$$

Each of these element shapes is a parallelepiped with two right angles. Now, from [Nadler and Rubin 2003] it follows that for these element shapes the reference geometry is characterized by

$$V = H_1 H_2 H_3, \qquad V^i = 0 \quad (i = 1, 2, 3, 4), \tag{3.5}$$

and the position vector X^* in (2.2) and the Cartesian coordinates $X_i^{*\prime}$ can be expressed in the forms

$$X^* = \sum_{j=1}^{3} \theta^j D_j, \qquad X_i^{*\prime} = \sum_{j=1}^{3} \theta^j (e_i' \cdot D_j). \tag{3.6}$$

Consequently, the exact displacements $\boldsymbol{u}^*$ and stresses $\boldsymbol{T}^*$ in (3.1) and (3.2) can be rewritten as functions of the convected coordinates θ^i $(i = 1, 2, 3)$.

Within the context of the linear theory of a CPE [Nadler and Rubin 2003] the director displacements $\boldsymbol{\delta}_i$ are defined such that

$$d_i = D_i + \delta_i, \quad (i = 0, 1, \ldots, 7), \tag{3.7}$$

and for the special elements defined by (3.3) the linearized forms of the inhomogeneous strains $\boldsymbol{\beta}_i$ become

$$\boldsymbol{\beta}_i = \boldsymbol{\delta}_{i+3} \quad (i = 1, 2, 3, 4). \tag{3.8}$$

As explained in [Nadler and Rubin 2003], the values $\boldsymbol{\delta}_i^*$ of the element director displacements $\boldsymbol{\delta}_i$ which correspond to the exact displacement field $\boldsymbol{u}^*$ need to be properly defined. Specifically, for these element shapes the values $\boldsymbol{\delta}_i^*$ are determined by the equations in [Nadler and Rubin 2003] which connect $\boldsymbol{\delta}_i^*$ to integrals over the reference element region of derivatives of $\boldsymbol{u}^*$ with respect to the convected coordinates. In particular, for the exact solutions (3.1) and (3.2) and the element shapes (3.3) it can be shown that these expressions yield

$$\boldsymbol{\delta}_1^* = \boldsymbol{\delta}_2^* = \boldsymbol{\delta}_3^* = \boldsymbol{\delta}_7^* = 0, \tag{3.9}$$

so that when $\boldsymbol{\delta}_i$ are replaced by the exact values $\boldsymbol{\delta}_i^*$ the linearized values of κ_4^i vanish

$$\kappa_4^1 = \kappa_4^2 = \kappa_4^3 = 0, \tag{3.10}$$

and the linearized forms of the constitutive equations (2.13) and (2.14) reduce to

$$\begin{aligned}
d^{1/2}\boldsymbol{T} &= 0, \qquad \boldsymbol{t}^i = 0 \quad (i = 0, 1, 2, 3, 7), \\[1mm]
\boldsymbol{t}^4 &= \left(m\frac{\partial \Psi}{\partial b_1} H_2 \boldsymbol{D}^1 + m\frac{\partial \Psi}{\partial b_3} H_1 \boldsymbol{D}^2 + m\frac{\partial \Psi}{\partial b_7} H_3 \boldsymbol{D}^3 \right), \\[1mm]
\boldsymbol{t}^5 &= \left(m\frac{\partial \Psi}{\partial b_5} H_3 \boldsymbol{D}^1 + m\frac{\partial \Psi}{\partial b_8} H_2 \boldsymbol{D}^2 + m\frac{\partial \Psi}{\partial b_4} H_1 \boldsymbol{D}^3 \right), \\[1mm]
\boldsymbol{t}^6 &= \left(m\frac{\partial \Psi}{\partial b_9} H_1 \boldsymbol{D}^1 + m\frac{\partial \Psi}{\partial b_6} H_3 \boldsymbol{D}^2 + m\frac{\partial \Psi}{\partial b_2} H_2 \boldsymbol{D}^3 \right)
\end{aligned} \tag{3.11}$$

where $\boldsymbol{d}^i$ have been replaced by the reference values $\boldsymbol{D}^i$. Also, the values of $\boldsymbol{m}^i$ in (2.21) associated with the exact solutions (3.1) and (3.2) are given by

$$\boldsymbol{m}^i = 0 \quad (i = 0, 1, 2, 3, 7), \qquad \boldsymbol{m}^i = \int_{\partial P_0} N^i \boldsymbol{T}^* \boldsymbol{N}^* dA^* \quad (i = 4, 5, 6), \tag{3.12}$$

where ∂P_0 is the reference boundary of the CPE, $\boldsymbol{N}^*$ is the unit outward normal to ∂P_0 and dA^* is the reference element of area. It then follows that within the context of the linearized theory, the equations of equilibrium associated with the bending (3.1) and torsion (3.2) solutions reduce to three vector equations

$$\boldsymbol{t}^i - \boldsymbol{m}^i = 0 \quad (i = 4, 5, 6). \tag{3.13}$$

Analytical expressions for B_{ij} can be developed by matching the solutions (3.1) and (3.2) for each of the element shapes (3.3). Then, the resulting coefficients are combined in a manner that ensures that B_{ij}

is a positive definite tensor. Specifically, with reference to the element shape E1 in (3.3a) consider six bending solutions associated with specifications of the orientation of e'_i relative to D_i

$$\text{Bending B1}: \quad e'_1 = D_1, \quad e'_3 = D_3, \tag{3.14a}$$

$$\text{Bending B2}: \quad e'_1 = D_1, \quad e'_2 = D_3 \tag{3.14b}$$

$$\text{Bending B3}: \quad e'_1 = D_2, \quad e'_3 = D_3 \tag{3.14c}$$

$$\text{Bending B4}: \quad e'_1 = D_2, \quad e'_2 = D_3 \tag{3.14d}$$

$$\text{Bending B5}: \quad e'_1 = D_3, \quad e'_3 = D_2 \tag{3.14e}$$

$$\text{Bending B6}: \quad e'_1 = D_3, \quad e'_3 = -D_1 \tag{3.14f}$$

Also, consider two torsion solutions associated with specifications

$$\text{Torsion T1}: \quad e'_1 = D_1, \quad e'_3 = D_3, \tag{3.15a}$$

$$\text{Torsion T2}: \quad e'_1 = D_2, \quad e'_3 = D_3, \tag{3.15b}$$

For each bending and torsion solution the exact displacements u^* are used to determine the exact values δ_i^*. Then, the linearized values of κ_j^i are determined using (2.9) and (3.8) with δ_i replaced by δ_i^* and the resulting constitutive equations for t^i are determined by (3.11). Similarly, the values of m^i are determined by using the exact stress T^* in the equations (3.12). Also, the values of the warping constant ϕ which corresponds to nearly pure torsion [Jabareen and Rubin 2008c] are determined by

$$\text{Torsion T1}: \quad m^6 \cdot D_1 = 0 \Rightarrow \phi = \frac{H_2^2(1 - D_{12}^2) - H_3^2}{H_2^2(1 - D_{12}^2) + H_3^2}, \tag{3.16a}$$

$$\text{Torsion T2}: \quad m^5 \cdot D_2 = 0 \Rightarrow \phi = \frac{H_1^2(1 - D_{12}^2) - H_3^2}{H_1^2(1 - D_{12}^2) + H_3^2}, \tag{3.16b}$$

In these expressions it can be seen that $\{m^6, D_1\}$ are associated with the cross-sectional coordinates $\{\theta^2, \theta^3\}$ and $\{m^5, D_2\}$ are associated with the cross-sectional coordinates $\{\theta^1, \theta^3\}$. With reference to Figure 2 it can also be seen that these expressions are similar to those in [Nadler and Rubin 2003] since the cross-section normal to D_1 has lengths $\{H_2\sqrt{1 - D_{12}^2}, H_3\}$ and the cross-section normal to D_2 has
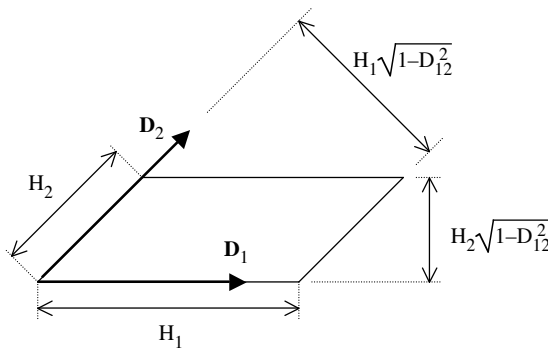
Figure 2. Cross-section of the parallelepiped element E1.

lengths $\{H_1\sqrt{1 - D_{12}^2}, H_3\}$. For each bending solution the value of γ can be eliminated in the resulting equations of equilibrium (3.13) and the value of ω can be eliminated from each of the equations of equilibrium associated with the torsion solutions. Also, the values (3.16) are used in the resulting torsion equations. It therefore follows that the each of the solutions (B1)-(B6), (T1) and (T2) yield nine scalar equations of equilibrium which total 72 scalar equations to determine the values of B_{ij} as functions of H_i and D_{12}. Some of these scalar equations are trivially satisfied and others are redundant. In particular, using a symbolic program like Maple it can be shown that the equations associated with the bending solutions (3.14) can be solved for B_{ij} ($i, j = 1, 2, \ldots, 5$) in terms of

$$\{B_{77}, B_{78}, B_{79}, B_{88}, B_{89}, B_{99}\}. \tag{3.17}$$

Then, these expressions can be substituted into the equations for torsion to determine all of the values of B_{ij} ($i, j = 1, 2, \ldots, 9$) in terms of one of the values $\{B_{77}, B_{88}, B_{99}\}$, say B_{77}.

Next, it is noted that that the strain energy function Ψ in (2.11) will be positive definite provided that the coefficient matrix B_{ij} is positive definite. The results of the calculations just described yield a form for B_{ij} which separates into two matrices [B_{ij} ($i, j = 1, 2, 3, 4$) and B_{ij} ($i, j = 5, 6, \ldots, 9$)]. In particular, it can be shown that

$$\det(B_{ij}) = (1 - v)^2(1 + v)^2(1 - D_{12}^2)^2 > 0, \quad (i, j = 1, 2, 3, 4) \tag{3.18}$$

which is independent of the lengths H_i and is positive for the full range of Poisson's ratio and D_{12}

$$-1 < v < \tfrac{1}{2}, \quad -1 < D_{12} < 1. \tag{3.19}$$

Moreover, the $\det(B_{ij})$ for ($i, j = 5, 6, \ldots, 9$) is a linear function of B_{77}, which has the value

$$\det(B_{ij}) = \tfrac{1}{2}(1 - v)^4(1 + v) \text{ for } \quad (i, j = 5, 6, \ldots, 9) \quad \text{and} \quad D_{12} = 0. \tag{3.20}$$

It was found that if the value of B_{77} is specified so that

$$\det(B_{ij}) = \tfrac{1}{2}(1 - v)^4(1 + v)(1 - D_{12}^2) \quad \text{for } (i, j = 5, 6, \ldots, 9), \tag{3.21}$$

then the expressions for B_{ij} are quite simple and

$$\det(B_{ij}) = \tfrac{1}{2}(1 - v)^6(1 + v)^3(1 - D_{12}^2)^3 \quad \text{for } (i, j = 1, 2, \ldots, 9), \tag{3.22}$$

which is positive for the range of values (3.19).

Similar procedures can be used to define bending and torsion solutions for the element shapes E2 and E3 and the resulting equations can be solved for B_{ij} to determine the dependence on the metrics D_{13} and D_{23}. Next, define auxiliary variables $\{\lambda_{12}, \lambda_{13}, \lambda_{23}\}$ as follows:

For $D_{12}^2 + D_{13}^2 + D_{23}^2 = 0$:

$$\lambda_{12} = \lambda_{13} = \lambda_{23} = 0, \tag{3.23a}$$

For $D_{12}^2 + D_{13}^2 + D_{23}^2 > 0$:

$$\lambda_{12} = \frac{D_{12}^2}{D_{12}^2 + D_{13}^2 + D_{23}^2}, \lambda_{13} = \frac{D_{13}^2}{D_{12}^2 + D_{13}^2 + D_{23}^2}, \lambda_{23} = \frac{D_{23}^2}{D_{12}^2 + D_{13}^2 + D_{23}^2}. \tag{3.23b}$$

Then it is possible to denote the values of B_{ij} associated with the solutions of the three elements E1-E3 in (3.3) by B_{ij}^{12} for E1, by B_{ij}^{13} for E2, and by B_{ij}^{23} for E3. Moreover, the matrix B_{ij}^0 is defined so that it yields a strain energy function Ψ equivalent to that obtained in [Nadler and Rubin 2003] for a rectangular parallelepiped, when the value of the torsion function $b^*(1)$ is taken to be $1/2$ as suggested in [Jabareen and Rubin 2008c]. Then, the general expression $B_{ij}(D_{12}, D_{13}, D_{23})$ combining these solutions is

$$B_{ij}(D_{12}, D_{13}, D_{23}) = (1 - \lambda_{12} - \lambda_{13} - \lambda_{23})B_{ij}^0 + \lambda_{12}B_{ij}^{12} + \lambda_{13}B_{ij}^{13} + \lambda_{23}B_{ij}^{23}. \qquad (3.24)$$

Now, using the definitions (3.23) it follows that each of the coefficients $\{(1 - \lambda_{12} - \lambda_{13} - \lambda_{23}), \lambda_{12}, \lambda_{13}, \lambda_{23}\}$ is non-negative and that at least one of them is positive. Also, each of the matrices $\{B_{ij}^0, B_{ij}^{12}, B_{ij}^{13}, B_{ij}^{23}\}$, given in Appendix A, is positive definite so that the combined matrix $B_{ij}(D_{12}, D_{13}, D_{23})$ is also positive definite for all reference element shapes.

4. Examples

For planar problems (in the D_1-D_2 plane with $D_{13} = D_{23} = 0$) it was shown in [Jabareen and Rubin 2008a] that

$$b_5 = b_6 = b_7 = b_8 = b_9 = b_{10} = b_{11} = 0. \qquad (4.1)$$

Moreover, since the values of B_{ij} $(i, j = 1, 2, 3, 4)$ for these planar problems reduce to those of the improved CPE in [Jabareen and Rubin 2007b], the results of the improved and generalized CPE will be identical for all planar problems. Consequently, the results of the example problems of a Cook's membrane, a Kirsch problem and buckling of a block considered in [Jabareen and Rubin 2007a; 2007b] are identical to those that would be predicted by the generalized CPE of Sections 2 and 3. In particular, it follows that the generalized CPE is free of the unphysical hourglassing that is predicted by the elements in ABAQUS, ADINA, ANSYS and FEAP [Taylor 2005] based on enhanced strain and incompatible mode methods.

In this section a number of example problems are considered to examine the predictions of the generalized CPE which show that it is more accurate than the improved CPE in [Jabareen and Rubin 2007b]. For all of the example problems the full nonlinear equations are solved using the constitutive equations (2.13) and (2.14) with strain energy specified by (2.8), (2.13), (2.14) and (2.18), even when the loads are small and the deformations remain small. Also, for irregular shaped elements the values of V^i in (2.7) and (2.13) can be nonzero so the response is examined for more general conditions than those used in the last section used to develop expressions for the constitutive coefficients B_{ij}. Unless otherwise stated the material is taken to be compressible with

$$K = 1\,\text{GPa}, \qquad \mu = 0.6\,\text{GPa}, \qquad \nu = 0.25. \qquad (4.2)$$

For the special examples which consider a nearly incompressible the material constants are specified by

$$K = 1000\,\text{GPa}, \qquad \mu = 0.6\,\text{GPa}, \qquad \nu \approx 0.4997. \qquad (4.3)$$

Furthermore, it was shown in [Jabareen and Rubin 2007a; 2007b] that the enhanced strain element in FEAP produces results similar to the enhanced strain or incompatible mode elements in ABAQUS, ADINA and ANSYS so that comparison with these types of elements will be limited to the element in FEAP.

For the calculations with the improved CPE presented here use is made of the modified torsion coefficients discussed in [Jabareen and Rubin 2008c]. In addition, for the improved CPE the matrices B_{ij} associated with the individual metrics $\{D_{12}, D_{13}, D_{23}\}$ are combined using an expression of the form (3.24) instead of using the method described in [Jabareen and Rubin 2007b] for ensuring that B_{ij} remains positive definite.

Furthermore, in the following figures the symbols {G, I, F, Q1, Q1P0, HO9} denote predictions of: the generalized CPE developed here; the improved CPE developed in [Jabareen and Rubin 2007b]; the enhanced strain, full integration, mixed element for nearly incompressible materials and the mixed higher order 9 node quadrilateral in FEAP, respectively. Also, it is noted that when the elements are rectangular parallelepipeds with ($D_{12} = D_{13} = D_{23} = 0$) the predictions of (G) and (I) are identical.

4.1. *Shear load on a thin cantilever beam (small deformations).* Figure 3 shows a sketch of a thin cantilever beam with dimensions

$$L = 200\,\text{mm}, \qquad H = W = 10\,\text{mm}, \tag{4.4}$$

which is fully clamped at its end $X_1^* = 0$ and is subjected to a shear force P (modeled by a uniform shear stress) applied in the e_2 direction to its end $X_1^* = L$. The lateral surfaces are traction free. The mesh $\{20n \times n \times n\}$ is defined by distorting the middle cross-section in its reference configuration (using the parameters a_1, a_2, a_3, a_4 shown in Figure 3), with $10n$ elements on each side of this cross-section and n elements in each of the e_2 and e_3 directions. Two cases of element distortion are considered:

$$\begin{aligned} \text{Case I:} &\quad a_1 = a, \;\; a_2 = -a, \;\; a_3 = a, \;\; a_4 = -a, \\ \text{Case II:} &\quad a_1 = a, \;\; a_2 = a, \;\; a_3 = -a, \;\; a_4 = -a, \end{aligned} \tag{4.5}$$

and the parameter a/H defines the element irregularity. Both of these cases cause the middle surface to remain planar with the normal to that surface being in the e_1-e_2 plane for Case I and in the e_1-e_3 plane for Case II. The value

$$u_{A2}^* = 0.21310\,\text{mm} \quad \text{for } P = 0.1\,\text{N} \tag{4.6}$$

of the e_2 component of the displacement of point A (see Figure 3) predicted by (G) with the most refined mesh ($n = 5$) and a regular mesh ($a/H = 0$) is considered to be exact and the error E associated with
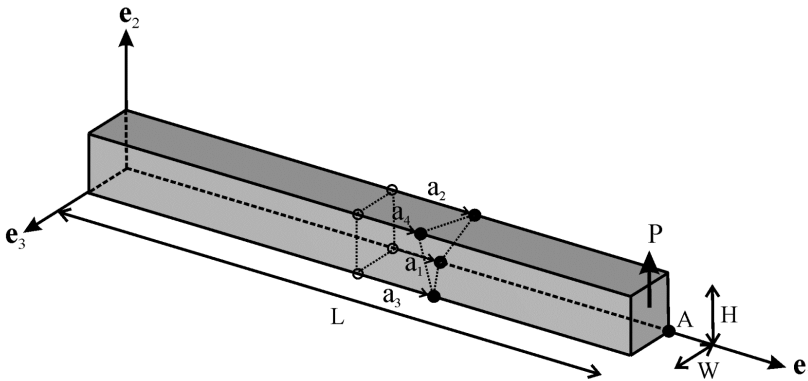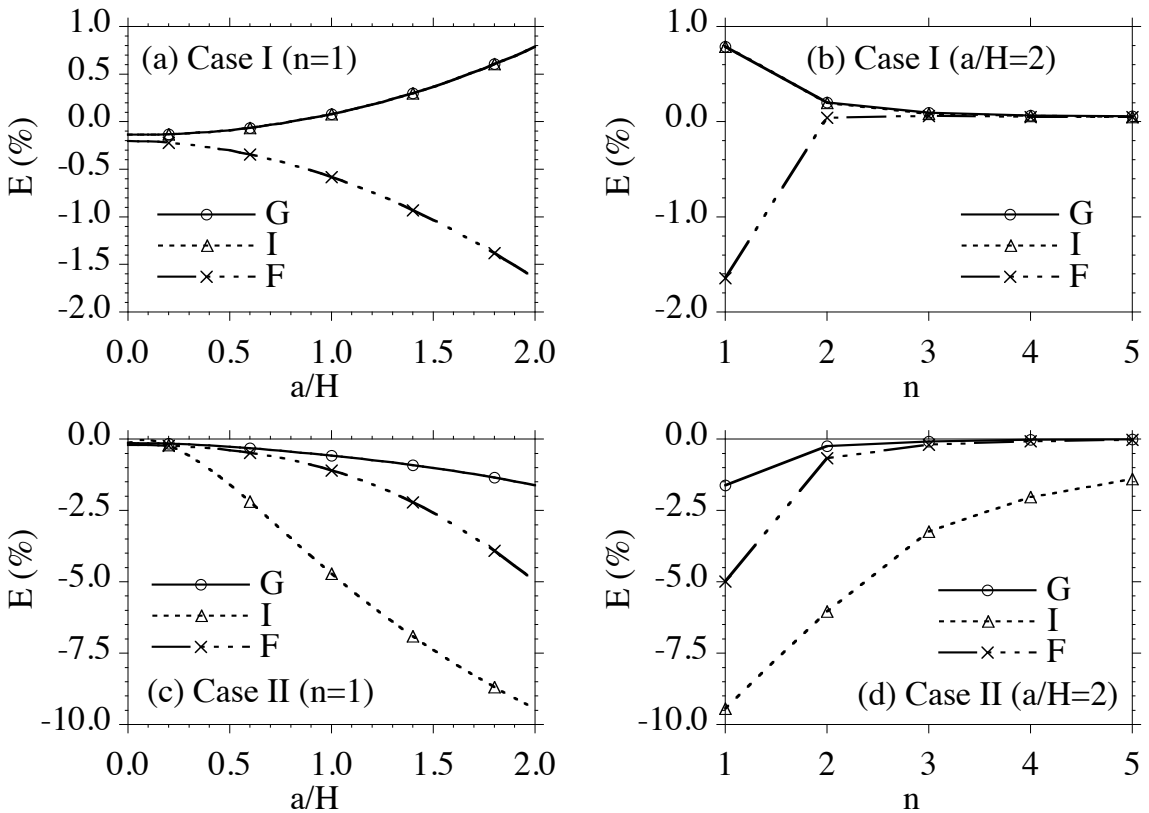

Figure 3. Shear load on a thin cantilever beam. The irregular element mesh is based on the distorted center cross-section.

the predictions u_{A2} of other calculations for the same value of P is defined by

$$E = \frac{u_{A2} - u^*_{A2}}{|u^*_{A2}|}. \tag{4.7}$$

Figure 4a shows the error as a function of the irregularity parameter a/H for Case I with $n = 1$. Ideally the response should be nearly insensitive to the value of a/H. This figure shows that the predictions of (G) and (I) are identical and are slightly more accurate than those of (F) for large values of irregularity. Figure 4b shows that the three elements converge to the same value for Case I with the refined mesh ($n = 5$) and large irregularity $a/H = 2$. The results for Case II shown in Figures 4c,d indicate that (G) is again slightly more accurate than (F) and that they both converge to the same solution. In contrast, Figures 4c,d show that (I) predicts significant errors and converges slowly for large irregularities. It will be shown later that this deficiency for Case II causes (I) to be inaccurate for out-of-plane bending of a rhombic plate.

Figure 4. Shear load on a thin cantilever beam (small deformations). (a,c) Errors in the displacement of the point A in the e_2 direction versus the distortion parameter a/H and; (b,d) the errors versus n for the mesh $\{20n \times n \times n\}$ defined for two cases of element distortion.
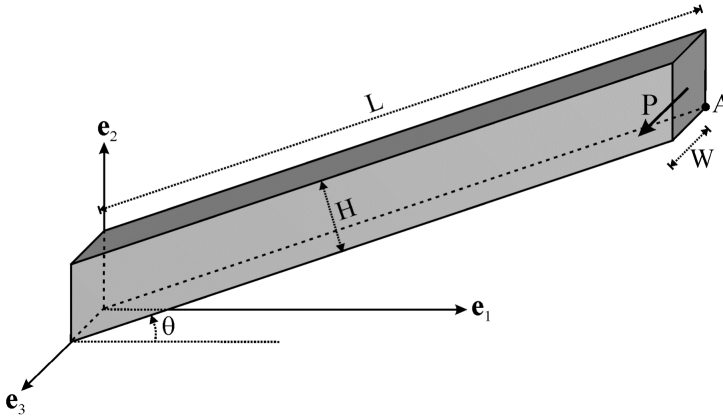
Figure 5. Shear load on a thin slanted cantilever beam.

4.2. *Shear load on a thin slanted cantilever beam (small deformations).*

Figure 5 shows a sketch of a thin slanted cantilever beam with dimensions (4.4) and with the slanting angle θ. The boundary conditions are the same as those for the previous example except that the shear load P is applied in the e_3 direction to emphasize differences between the predictions of (G) and (I). Again the mesh is taken to be $\{20n \times n \times n\}$ with $20n$ elements in axial direction of the beam. All of the elements have parallelogram cross-sections in the e_1-e_2 plane with sides parallel to the ends of the beam.

Figure 6a shows the displacement component u_{A3} of point A (see Figure 5) in the e_3 direction as a function of θ for the most refined mesh ($n = 5$). The error E in u_{A3} is defined in a similar manner to (4.7) with the exact value u_{A3}^* taken to be that predicted by (G) for each value of θ with $n = 5$ and with the load P given by (4.6). Figures 6b,c show that (G) and (F) converge to the same values and that (G) is slightly more accurate than (F) for n=1 and large values of θ. Also, it can be seen that (I) predicts significant errors with slow convergence.

4.3. *Shear load on a thin twisted cantilever beam (small deformations).*

The problem of shear loading of a thin twisted beam provides a severe test of the accuracy of an element formulation since the elements have irregular shapes and the response couples torsion and bending modes of deformation. In its unstressed reference configuration the twisted beam has length L and a rectangular cross-section with height H and width W given by

$$L = 200\,\text{mm}, \qquad H = 10\,\text{mm}, \qquad W = 2\,\text{mm}. \tag{4.8}$$

Also, each of the cross-sections is twisted by the angle θ such that the position of a material point X^* in the reference configuration is given by

$$X^* = X_i^{*\prime} e_i', \qquad \theta = \frac{X_1^{*\prime}}{L}\Theta,$$

$$e_1' = e_1, \qquad e_2' = \cos\theta\, e_2 + \sin\theta\, e_3, \qquad e_3' = -\sin\theta\, e_2 + \cos\theta\, e_3, \tag{4.9}$$

where Θ controls the magnitude of the twist. Furthermore, the influence of irregular element meshes is explored by applying the twist θ to the cross-sections of the beam shown in Figure 3 and in Figure 7 using the element irregularity specified by Case I in (4.5). The surface $X_1^{*\prime} = 0$ is fully clamped, a shear
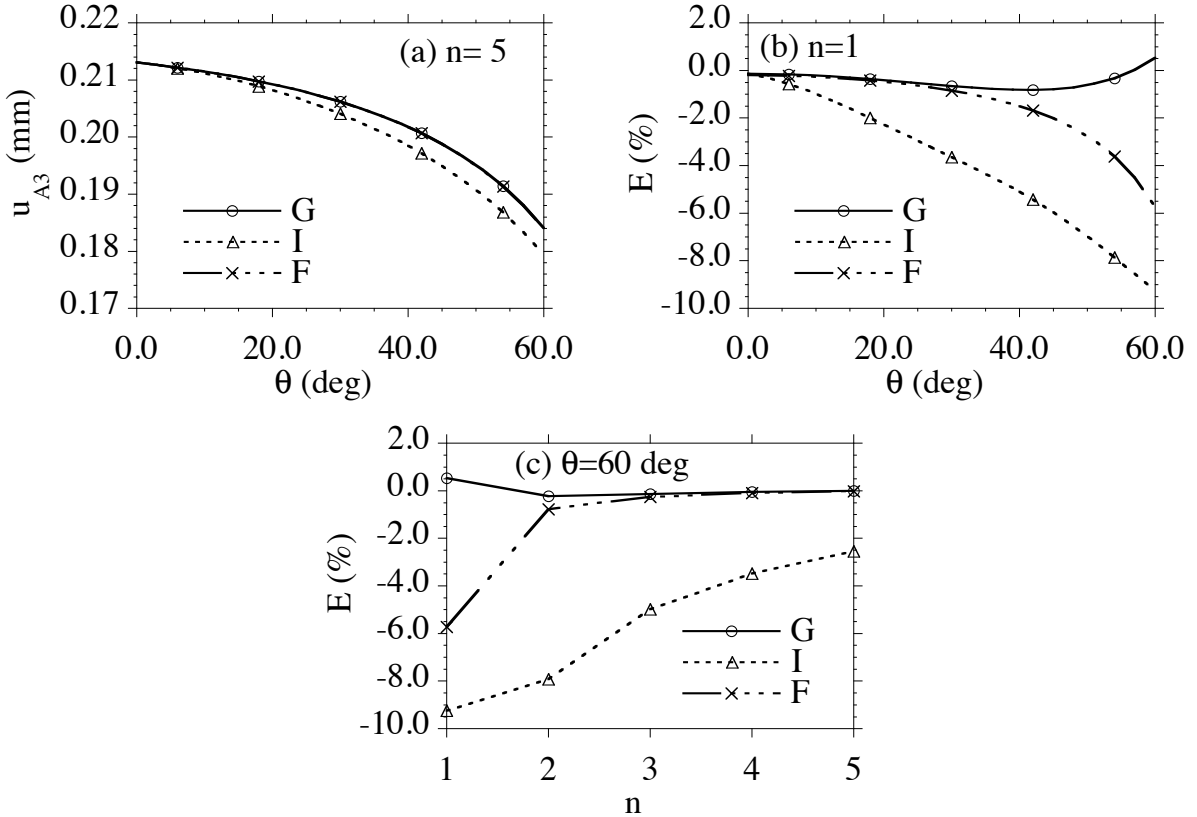
Figure 6. Shear load on a thin slanted cantilever beam (small deformations). (a) Displacement u_{A3} of the point A in the $\boldsymbol{e}_3$ direction versus the angle θ for $n = 5$ with the mesh $\{20\,n \times n \times n\}$; (b) errors in u_{A3} versus θ for $n = 1$; (c) errors in u_{A3} versus n for $\theta = 60$ deg.

force P (modeled by a uniform shear stress) is applied to the end $X_1^{*\prime} = L$ in the constant $\boldsymbol{e}_2'$ direction (defined by its direction in the reference configuration) and the remaining lateral surfaces are traction free. Also, the element mesh for this problem is specified by $\{20\,n \times n \times n\}$ with $20n$ elements along the length of the beam.

Figure 8a shows the component u_{B2}' of the displacement of the point B (see Figure 7) in the $\boldsymbol{e}_2'$ direction

$$u_{B2}' = \boldsymbol{u}_B \cdot \boldsymbol{e}_2', \tag{4.10}$$

versus the pre-twist Θ for the most refined mesh with $n = 5$, no element irregularity ($a/H = 0$) and the load given by

$$P = 0.01\,\text{N}. \tag{4.11}$$

This value of load is used for all calculations in this subsection. It can be seen that $\{G, I, F\}$ converge to the same results. Thus, the value $u_{B2}'^*$ of u_{B2}' predicted by (G) for $n = 5$ is considered to be exact and the error E of other calculations is defined in a similar manner to (4.7). Figures 8b,c show the influence of element irregularity for the coarse mesh with $n = 1$ and Figures 8d,e consider a finer mesh
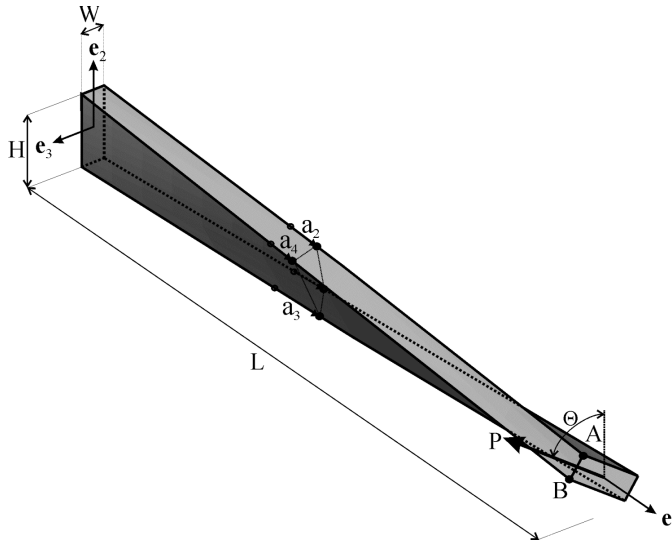
Figure 7. Shear load on a thin twisted cantilever beam. The element mesh is based on the distorted center cross-section.

with $n = 2$. From these figures it can be seen that (G) is as accurate as (F) and is much more accurate than (I), especially for irregular shaped elements.

4.4. *Lateral torsional buckling of a thin cantilever beam (large deformations).* For this example the beam and element mesh are characterized by the same parameters as used in Section 4.3 with the shear force P being applied in the e_2' direction. To investigate rotation of the beam's end it is convenient to consider the difference in the displacements of the points A and B shown in Figure 7. Specifically, the quantity Δu is defined by

$$\Delta u = (\boldsymbol{u}_B - \boldsymbol{u}_A) \cdot \boldsymbol{e}_2'. \tag{4.12}$$

Figure 9 shows the results for large deformation lateral torsional buckling of a thin cantilever beam. Again it is emphasized that the direction e_2' of the load is held constant during loading. The buckling process is triggered by the small pre-twist

$$\Theta = 0.1 \, \text{deg}, \tag{4.13}$$

which smoothes out the bifurcation that would occur for a perfect beam with $\Theta = 0$. Figure 10 shows the results for shear loading with a large pre-twist

$$\Theta = 30 \, \text{deg}. \tag{4.14}$$

Moreover, the curves in Figures 9 and 10 denoted by (E) are predicted by (G) with $n = 5$ and $a/H = 0$ and are considered to be exact.

The results in Figure 9 show that for $n = 2$ (Figures 9a,b) the predictions are not yet converged and are sensitive to element irregularity with large errors being predicted by (I). Figures 9c,d show that for $n = 3$ the predictions are reasonably converged and that the sensitivity of element irregularity is reduced for {G, F} but that (I) still predicts large errors.
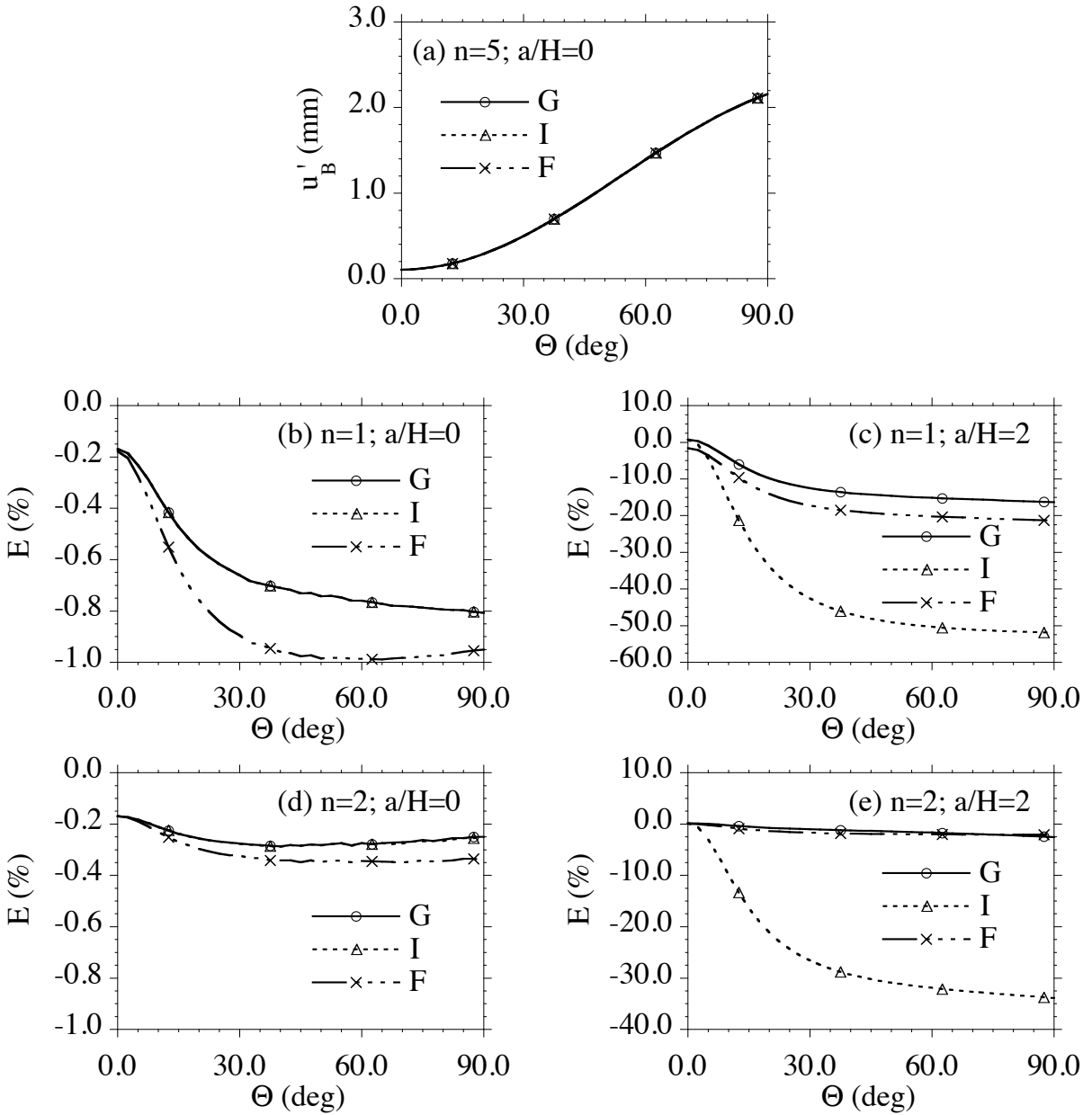
Figure 8. Shear loading of a thin twisted cantilever beam with a pre-twist Θ and the mesh $\{20\,n \times n \times n\}$ (small deformations). The influence of element irregularity is shown in the middle row graphs for $n = 1$ and in the bottom graphs for $n = 2$.

The results in Figure 10 for shearing of a thin cantilever beam with a large pre-twist again show that the predictions of $\{G, F\}$ are relatively accurate but that the predictions of (I) are inaccurate for the irregular shaped elements even for the mesh with $n = 3$ (Figure 10d). This result is consistent with that in [Jabareen and Rubin 2007b, Figure 8b], which showed that the error of out-of-plane bending of a beam
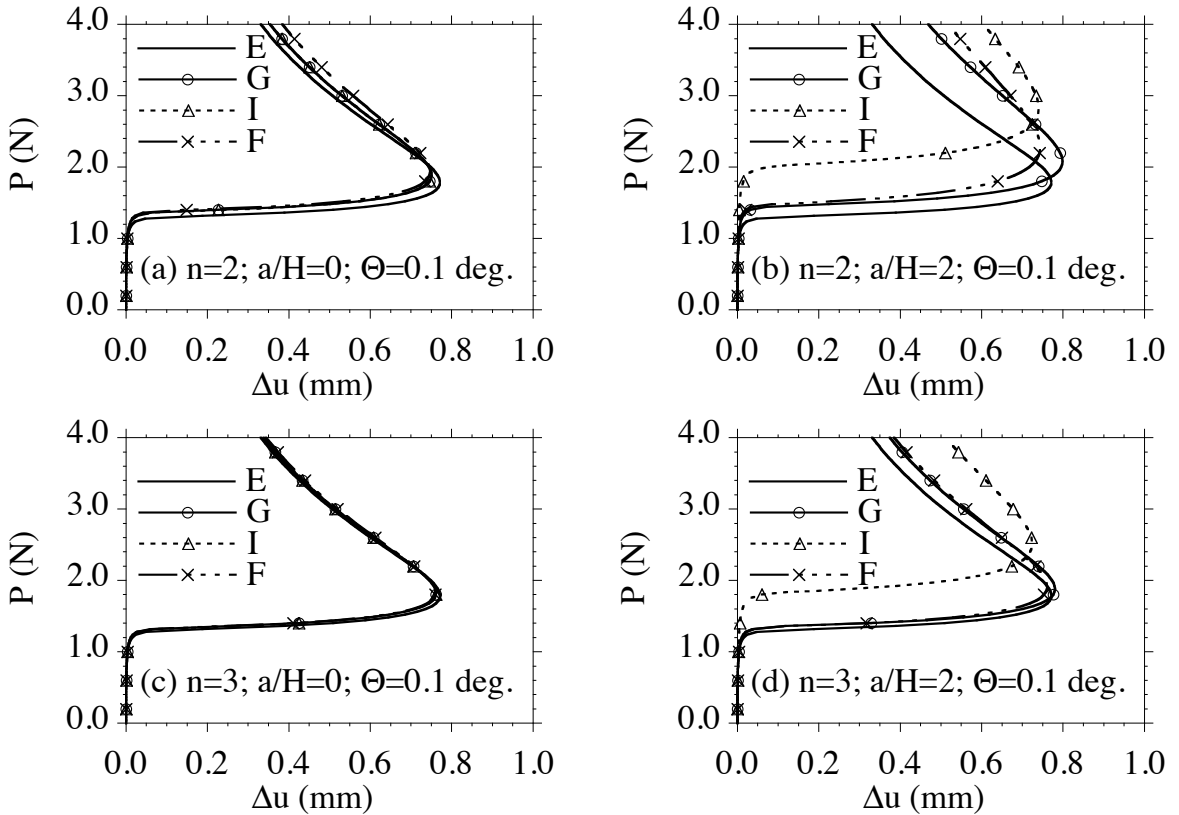
Figure 9. Large deformation lateral torsional buckling of a thin cantilever beam with a small pre-twist $\Theta = 0.1$ deg. using the mesh $\{20n \times n \times n\}$. The influence of element irregularity is shown in the top two graphs for $n = 2$ and in the bottom two for $n = 3$.

with the element irregularity of Case I [(4.5) here] does not have a zero slope as a/H approaches zero. Furthermore, this error causes (I) to predict inaccurate results for out-of-plane bending of a rhombic plate, as will be shown next.

4.5. *Point load on the corner of a thin partially clamped rhombic plate (small deformations).* Figure 11 shows a sketch of one quarter of a thin fully clamped rhombic plate with dimensions

$$L = 500 \, \text{mm}, \qquad H = 10 \, \text{mm}, \tag{4.15}$$

with two clamped and two free edges and which is loaded at its corner by a point force. The length of each edge is L and the load is specified by

$$P = 1 \, \text{N}. \tag{4.16}$$

The mesh used for the plate is defined by $\{10n \times 10n \times n\}$ with n elements through the thickness.

Figure 12a shows the component u_{A3} of the displacement of the point A in the $\boldsymbol{e}_3$ direction as a function of θ for the most refined mesh ($n = 5$). The error E in this displacement is defined in a similar
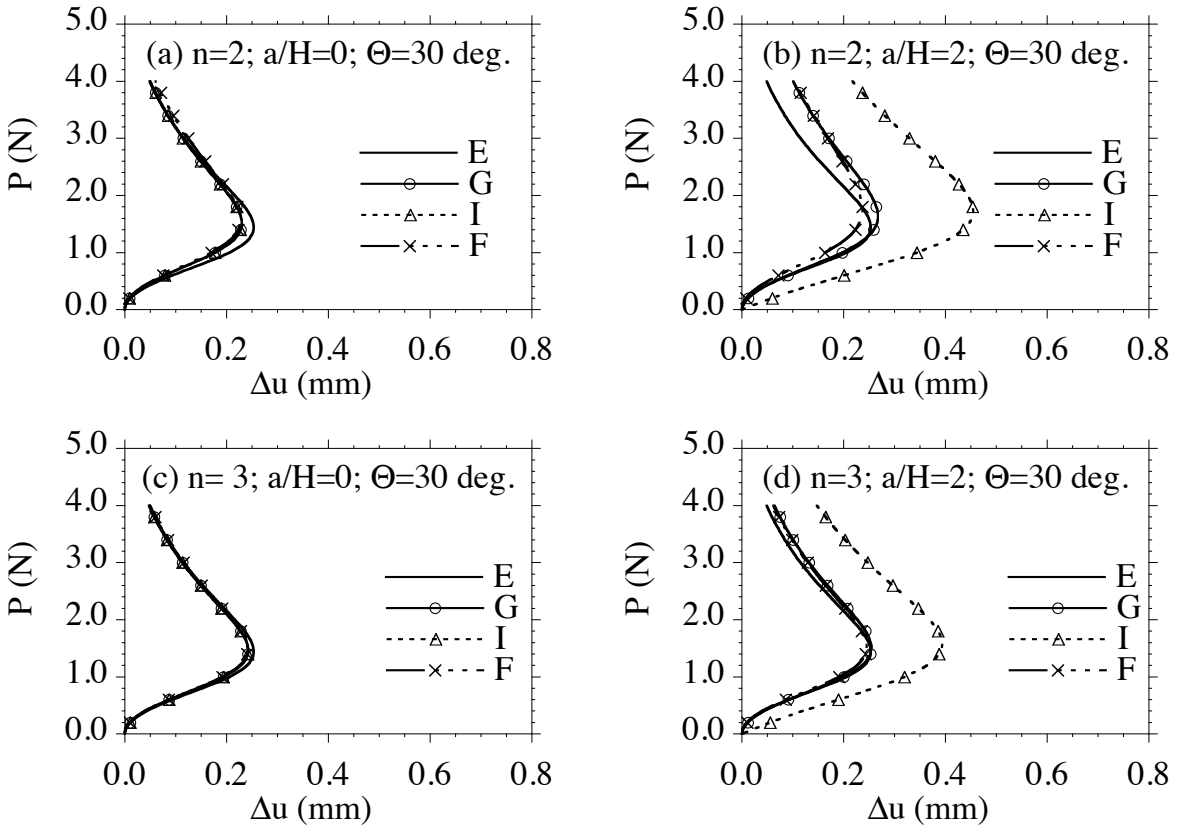
Figure 10. Large deformation shear loading of a thin cantilever beam with a pre-twist $\Theta = 30$ deg using the mesh $\{20\,n \times n \times n\}$. The influence of element irregularity is shown in the top two graphs for $n = 2$ and in the bottom two for $n = 3$.
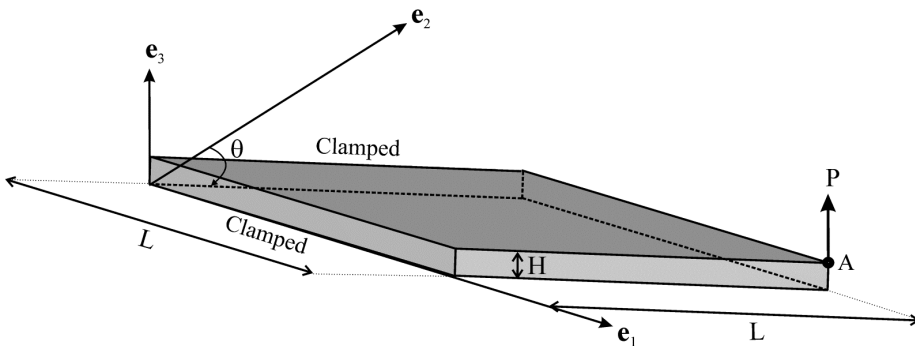

Figure 11. Point load on the corner of a thin partially clamped rhombic plate.

manner to (4.7) with the exact value u^*_{A3} taken to be that predicted by (G) for each value of θ with $n = 5$ and the load P given by (4.16). Figures 12b,c show that $\{G, F\}$ predict nearly the same values, that (I) predicts significant errors for $n = 1$ (especially for the angle $\theta = 60$ deg) and that (I) exhibits slow convergence.
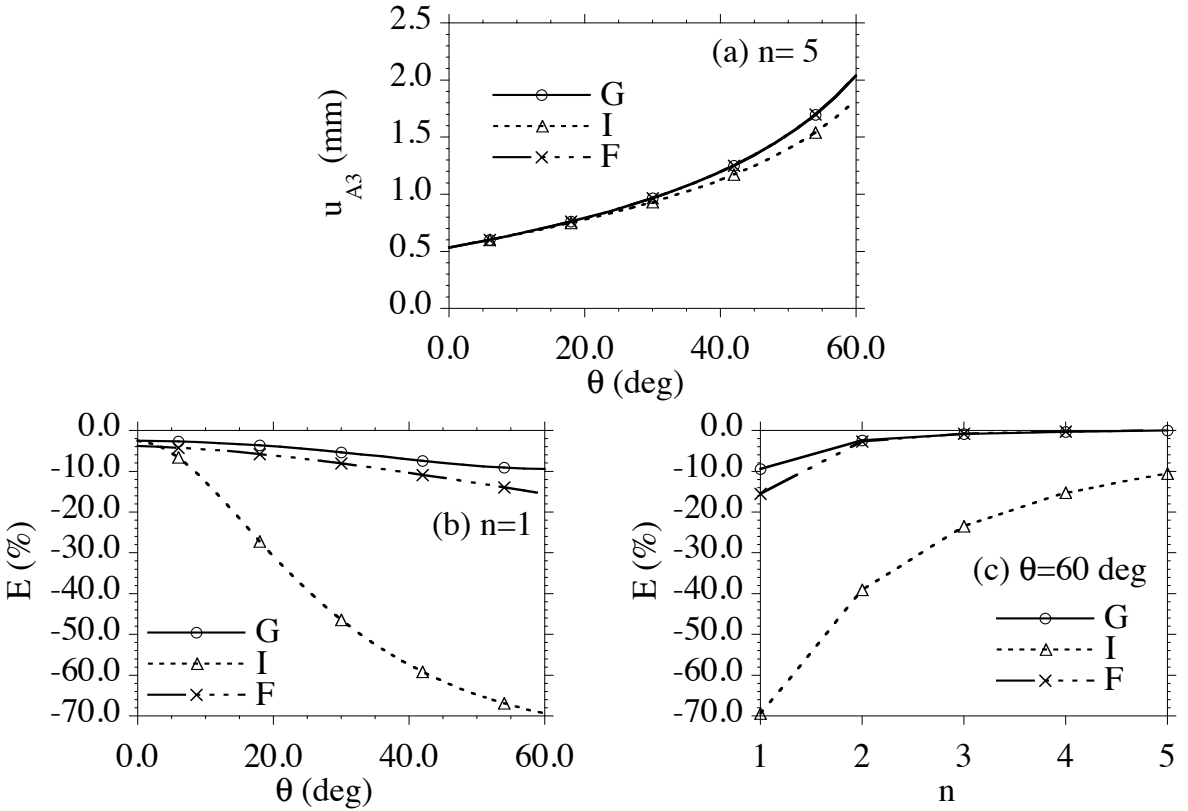
Figure 12. Point load on the center of a thin fully clamped rhombic plate (small deformations). Displacement u_{A3} of the point A in the e_3 direction versus the angle θ for $n = 5$ with the mesh $\{10\, n \times 10\, n \times n\}$; (b) errors in u_{A3} versus θ for $n = 1$; (c) errors in u_{A3} versus n for $\theta = 60$ deg.
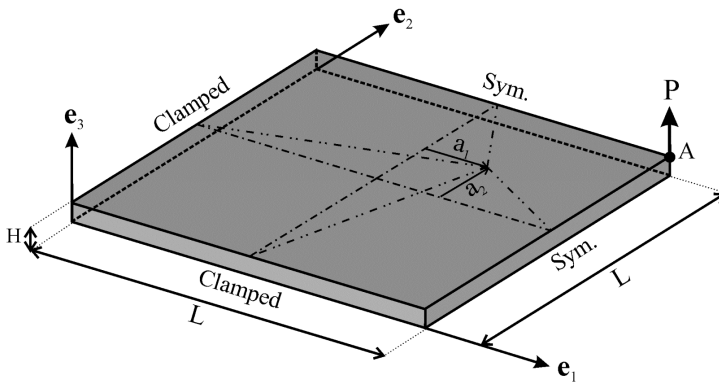
Figure 13. Point load on the center of a thin fully clamped square plate with an irregular element mesh.

4.6. *Point load on the center of a thin fully clamped square plate with an irregular element mesh (small deformations).* Figure 13 shows a sketch of one quarter of a thin fully clamped square plate with dimensions (4.8) that is loaded by a point force at its center. Only one quarter of the plate is modeled and

the value P given by (4.16) corresponds to one quarter of the load that would be applied to the center of the entire plate. Irregular elements are specified by moving the center point of the quarter section to the position characterized by the lengths $\{a_1, a_2\}$ (shown in Figure 13) defined by two cases:

$$\text{Case I: } a_1 = a_2 = a, \quad -1 \leq \frac{4a}{L} \leq 1,$$

$$\text{Case II: } a_1 = \frac{L}{4} \cos(\theta), \quad a_2 = \frac{L}{4} \sin(\theta), \quad 0 \leq \theta \leq 2\pi. \tag{4.17}$$

The quarter section of the plate is meshed by $\{10n \times 10n \times n\}$ with each subsection being meshed by $\{5n \times 5n \times n\}$ and with n elements through the thickness. The error E in the displacement component u_{A3} of point A in the e_3 direction is defined in a similar manner to (4.7) with the exact value u_{A3}^* taken to be that predicted by (G) for regular elements ($a/L = 0$) with $n = 5$

$$u_{A3}^* = 0.16893 \text{ mm} \quad \text{for } P = 1 \text{ N.} \tag{4.18}$$

Figures 14a,b show the error for $n = 1$ as a function of the irregularity parameters $4a/L$ for Case I (Figure 14a) and as a function of $\theta/(2\pi)$ for Case II (Figure 14b). From these figures it can be seen that that $\{G, F\}$ are relatively insensitive to the magnitude and type of element irregularity but that (I) predicts significant errors for irregular elements.

4.7. *Point load on the corner of a thin partially clamped rhombic plate (large deformations).* Figure 15 shows the deformed shapes of a thin partially clamped rhombic plate subjected to a point load on its corner for two different angles θ and the same value P of load. The plate is fully clamped on two edges and the other edges and major surfaces are traction free. The dimensions are given by (4.8) as shown in Figure 11 (with L now being the length of the plate's edge) and the point force P is specified by

$$P = 1 \text{ kN.} \tag{4.19}$$
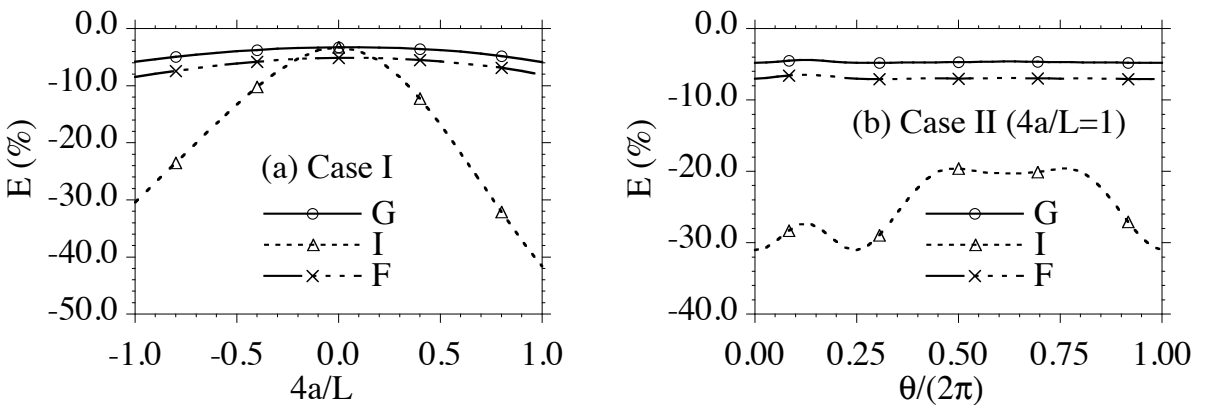
Figure 14. Point load on the center of a thin fully clamped square plate (small deformations). Errors in the displacement of the point A in the e_3 direction versus the distortion parameters (a) $4a/L$ and; (b) the angle θ for two cases of element irregularity with the mesh $\{10 \times 10 \times 1\}$.

(a) $\theta = 0$ deg   (b) $\theta = 60$ deg
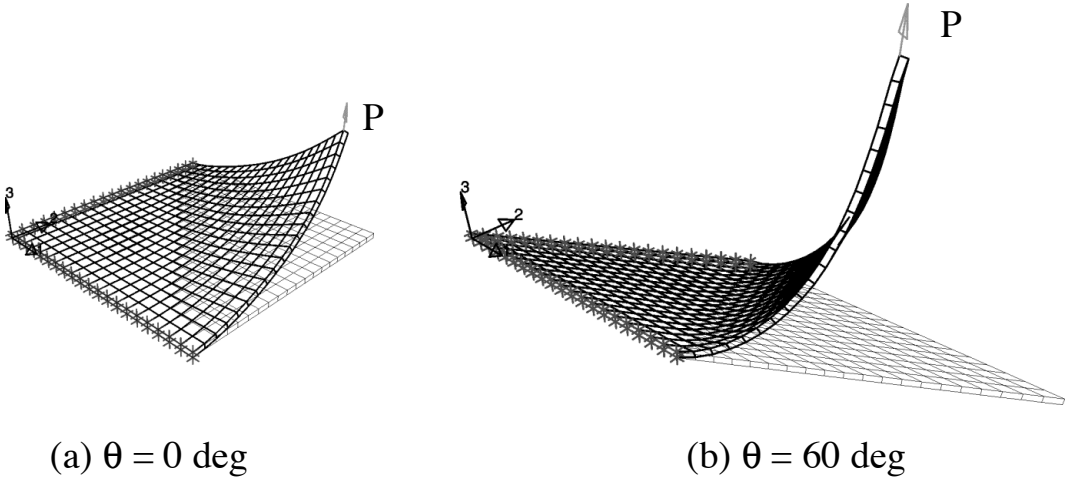
Figure 15. Point load on a partially clamped rhombic plate (large deformations). Predictions of the generalized CPE for the mesh $\{10\,n \times 10\,n \times 1\}$ with $n = 2$ and $P = 1\,\text{kN}$.

The mesh is specified by $\{10\,n \times 10\,n \times 1\}$ and the exact value u_3^* of the displacement of the corner in the e_3 direction is determined by the most refined solution (G) with $n = 5$

$$u_3^* = 0.21084\,\text{m} \quad \text{for } \theta = 0\,\text{deg}, \qquad u_3^* = 0.39306\,\text{m} \quad \text{for } \theta = 60\,\text{deg}. \qquad (4.20)$$

Figures 16 show the load P versus displacement curves for $n = 2$ and the convergence curves for two values of the angle θ. Comparison of Figures 16a,c shows that the rhombic plate with angle $\theta = 60$ deg is more flexible than that for $\theta = 0$ deg and that $\{G, F\}$ predict nearly the same values, whereas (I) predicts significant errors for the angle $\theta = 60$ deg. Also, Figure 16d shows that the convergence properties of (G) are slightly better than those of (F) for the case when $\theta = 60$ deg.

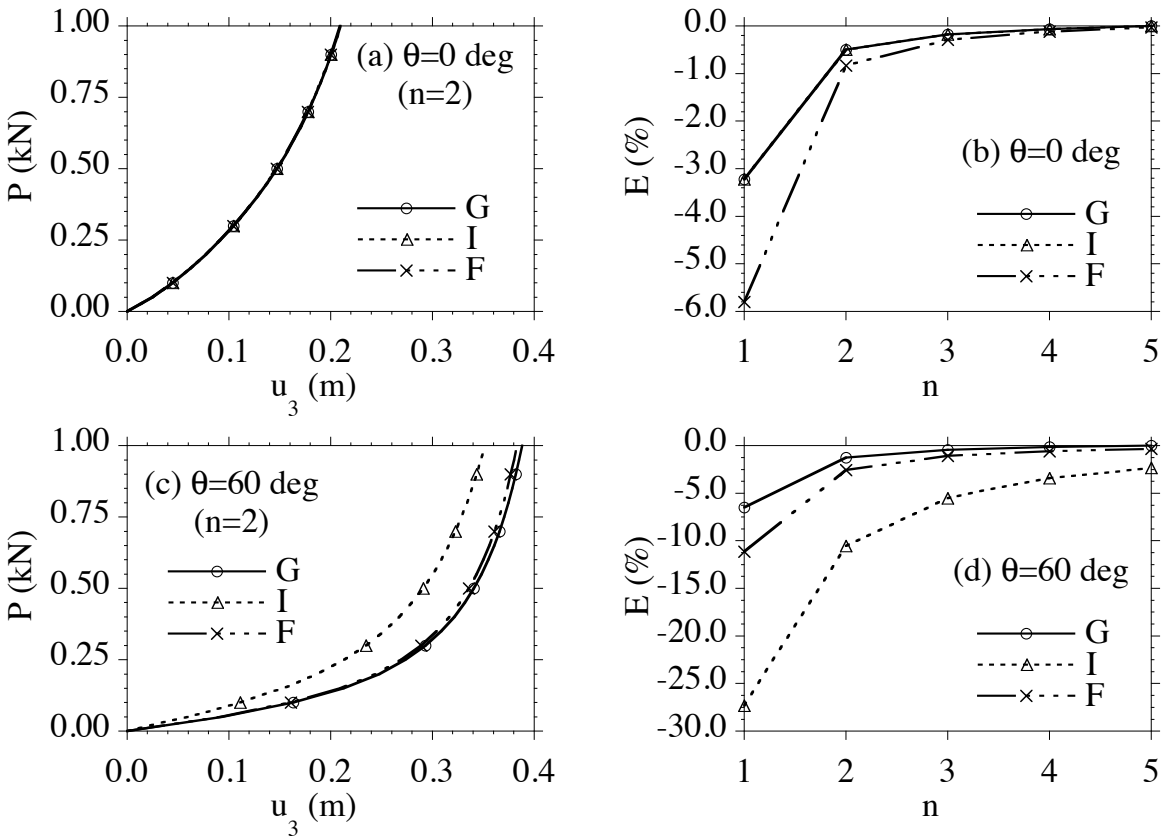### 4.8. A pair of opposing point loads applied to a complete circular cylindrical shell (large deformations).
Figure 17 is a sketch of one eighth of a thin circular cylindrical shell that is subjected to a pair of opposing point loads P. The entire shell has length $2L$, middle surface radius R, and thickness H, with

$$L = 300\,\text{mm}, \qquad R = 300\,\text{mm}, \qquad H = 3\,\text{mm}. \qquad (4.21)$$

All nodes (except for one) on the circular edges of the shell are allowed to move freely in the axial direction but their radial and circumferential positions are fixed. Also, the eighth region of the shell is modeled by the mesh $\{10\,n \times 10\,n \times 1\}$ in the axial, circumferential and radial directions, respectively.

Figure 18 plots the force P versus radial displacement u_r of the point A under the load for different mesh refinements. Curves are presented for (G) for the most refined mesh of $n = 10$ and for $\{G, F\}$ for $n = 3$ (Figure 18a) and $n = 5$ (Figure 18b). It can be seen from Figure 18a that for the coarser mesh ($n = 3$) the load-deflection curve exhibits ratcheting due to localized limit points whereas for the more refined mesh ($n = 5$) in Figure 18b the load-deflection curve is smooth. It can also be seen that the predictions of $\{G, F\}$ tend to converge to the same solutions. Figure 19 shows the deformed shape of one eighth of the circular shell predicted by (G) for $n = 5$ and $P = 1.73\,\text{kN}$ with no enhancement of the

Figure 16. Point load on a partially clamped rhombic plate (large deformations). Predictions of the load P versus displacement u_3 at the loaded corner and convergence of the error in the displacement for the mesh $\{10n \times 10n \times 1\}$ with the load $P = 1$ kN and different angles θ.
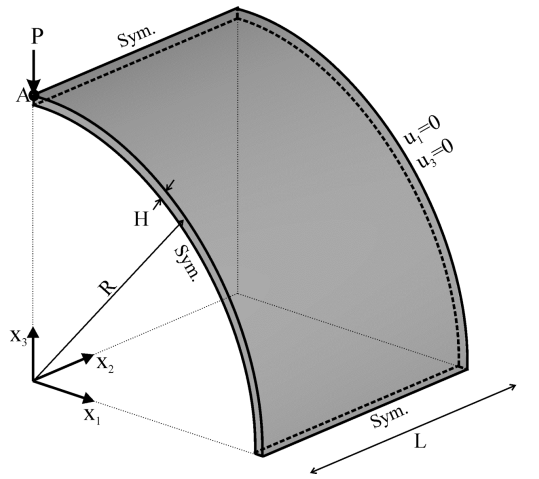
Figure 17. Sketch of one eighth of a thin circular cylindrical shell that is subjected to a pair of opposing point loads P.
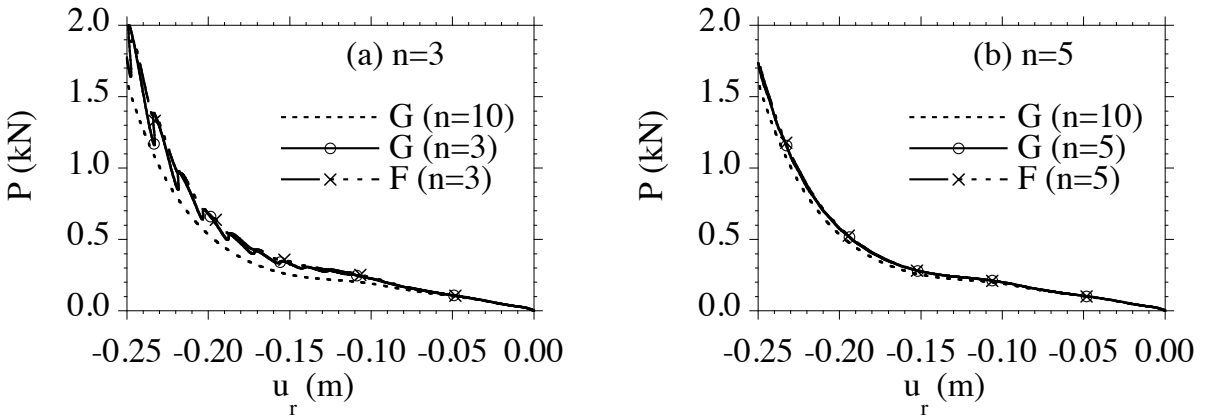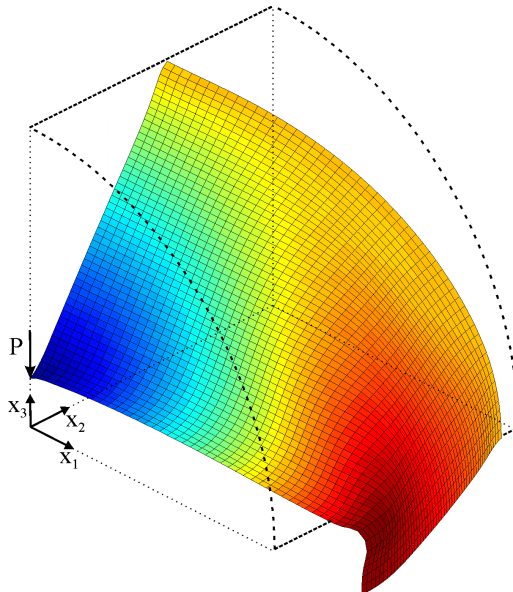
Figure 18. A pair of opposing concentrated loads P applied to a thin circular cylindrical shell with the mesh $\{10\,n \times 10\,n \times 1\}$.

displacements. In particular, it is noted that the inability of the coarse mesh to capture the high curvature of the middle of the shell far away from the load is most likely the cause of the ratcheting shown in Figure 18a.

4.9. *Plane strain indentation of a rigid plate into a nearly incompressible block (large deformations).* Crisfield et al. [1995] and César de Sá et al. [2001] considered the example of plane strain indentation of a rigid plate into a block and showed limitations of enhanced strain elements for elastic and elastic-plastic response. Figure 20 shows a sketch of the dimensions and boundary conditions for this problem with a

Figure 19. Deformed shape of an eighth of a thin circular cylindrical shell subjected to a pair of opposing concentrated point loads P for the mesh $\{10\,n \times 10\,n \times 1\}$ with $n = 5$ and $P = 1.73\,\text{kN}$.

nearly incompressible elastic material. The block has length $2L$, height L and depth W. Material points on its sides and bottom remain in contact with a rigid container and are allowed to slide freely. The top surface of the block is loaded by a rigid plate (AB) of length L which makes perfect contact with the block so that material points in contact with the rigid plate move only vertically. The remaining half of the block's top surface is traction free. The dimensions of the block are given by

$$L = W = 1 \, \text{m}. \tag{4.22}$$

Irregular meshes are defined by dividing the block into four subsections with the central node moving to the position characterized by the lengths $\{a_1, a_2\}$ (shown in Figure 20) defined by two cases:

$$\text{Case I:} \quad a_1 = a, \, a_2 = 0, \quad -1 \le \frac{8a}{3L} \le 1, \, u_{A2} = -0.1 \, \text{m}, \, n = 5,$$

$$\text{Case II:} \quad a_1 = 0, \, a_2 = a, \quad -1 \le \frac{8a}{3L} \le 1, \, u_{A2} = -0.1 \, \text{m}, \, n = 5. \tag{4.23}$$

The entire block is meshed by $\{8n \times 4n \times 1\}$ with $4n$ elements in the $\mathbf{e}_1$ direction and $2n$ elements in the $\mathbf{e}_2$ in each of the subsections. The point C (shown in Figure 20) is located on the free top surface at a distance $0.25L$ from the corner B of the rigid plate.

Figure 21 shows convergence of the solution for the regular ($a = 0$) mesh $\{8n \times 4n \times 1\}$ and $u_{A2} = -0.1 \, \text{m}$. The converged value u_{C2}^* of the displacement of the point C in the $\mathbf{e}_2$ direction predicted by (G) for a regular mesh with $n = 20$ is considered to be exact and is given by

$$u_{C2}^* = 0.071895 \, \text{m} \quad \text{for } u_{A2} = -0.1 \, \text{m with } n = 20. \tag{4.24}$$

The error E of in the values u_{C2} predicted by calculations of other elements and meshes is defined by an expression similar to (4.7). Figure 21 shows the convergence of this error predicted by {G, Q1P0, HO9}. This error is plotted relative to n for the mesh $\{8n \times 4n \times 1\}$ in Figure 21a and is plotted relative to the degrees of freedom (DOF, calculated for plane strain response) in Figure 21b. From Figure 21a it is not clear if (Q1P0) exhibits a locking behavior by converging to a value different from (G) or whether the
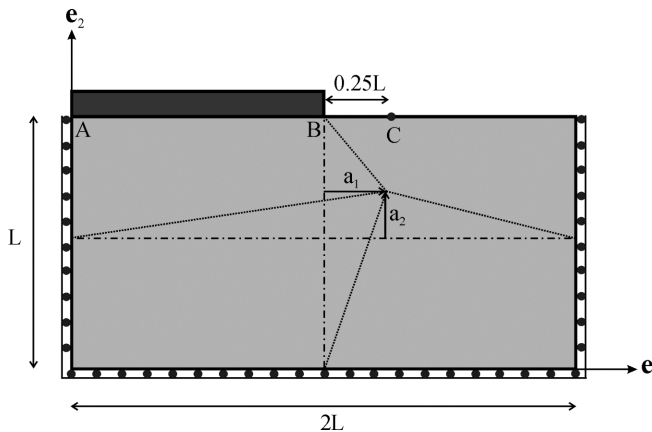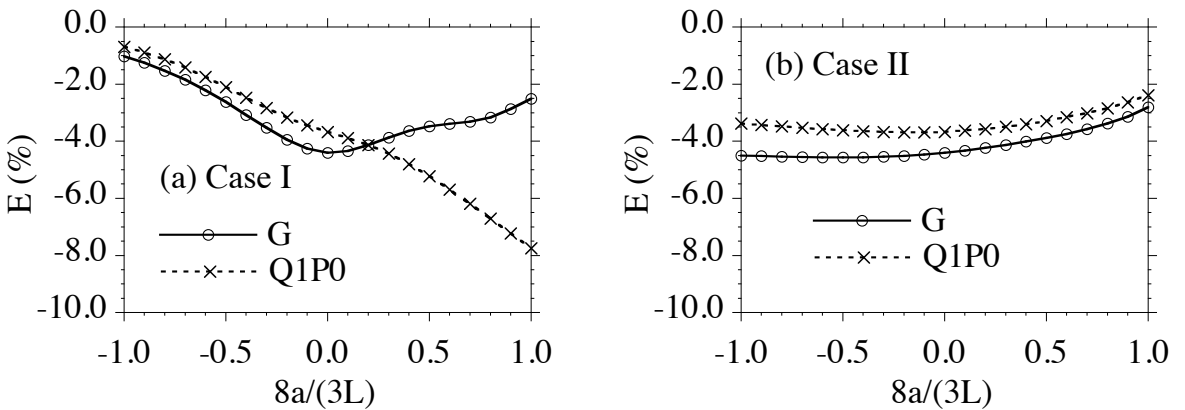

Figure 20. Plane strain indentation of a rigid plate into a block showing the boundary conditions and definition of element irregularity.
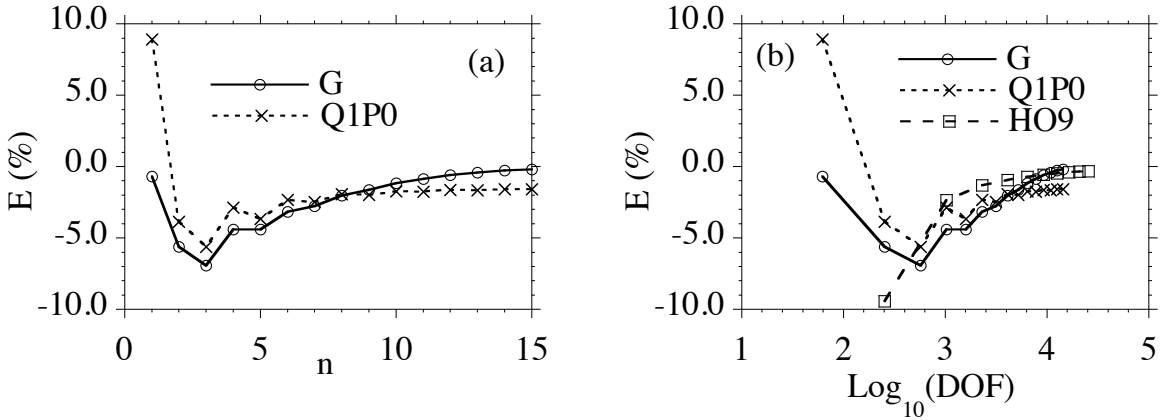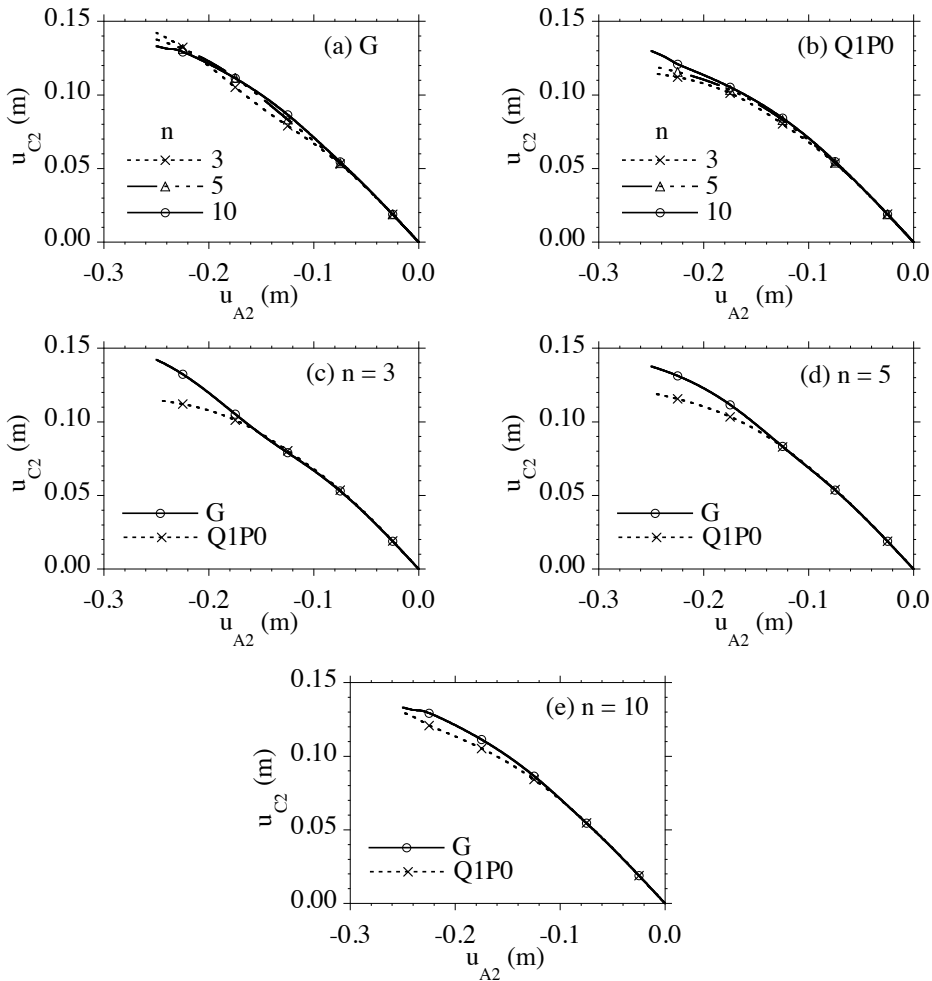
Figure 21. Plane strain indentation of a rigid plate into a nearly incompressible block. Convergence of the error E in the displacement u_{C2} of the point C using the regular mesh $\{8n \times 4n \times 1\}$ for $u_{A2} = -0.1$ m versus: (a) n; and (b) versus the number of degrees of freedom DOF.

convergence rate is very slow. To validate the converged value of (G) for $n = 20$, calculations were also performed using the mixed higher order element (HO9) with the mesh $\{8n \times 4n \times 1\}$ up to $n = 10$. In particular, it can be seen in Figure 21b that (HO9) tends to converge to the value predicted by (G).

Figure 22 presents the errors E in the displacement u_{C2} for two cases of element irregularity and for the mesh $\{8n \times 4n \times 1\}$ with $n = 5$ and $u_{A2} = -0.1$ m. Since there is a strain concentration near the edge of the plate it is expected that a non-fully converged solution will be sensitive to element irregularity. In particular, it can be seen from Figure 22a that (Q1P0) is more sensitive to element irregularity than (G) for positive values of a for Case I which cause the elements near the plate's edge B to be more irregular. The results in Figure 22b show that the error reduces slightly for increasing positive values of a for Case II which cause the elements near the plate's edge B to be more refined.

Figure 22. Plane strain indentation of a rigid plate into a nearly incompressible block. Error E in the displacement u_{C2} of the point C for two cases of element irregularity and for the mesh $\{8n \times 4n \times 1\}$ with $n = 5$ and $u_{A2} = -0.1$ m.
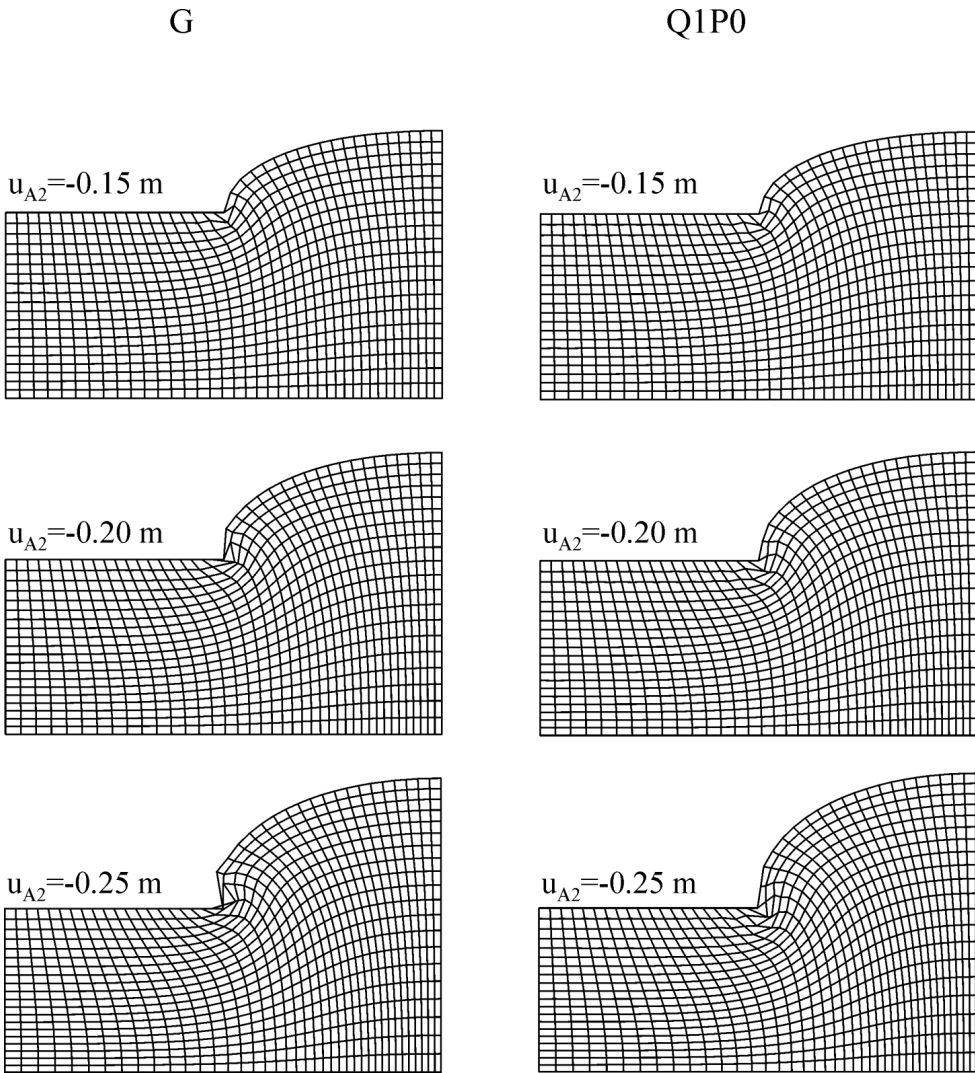
Figure 23. Plane strain indentation of a rigid plate into a nearly incompressible block showing nonlinear load curves using the regular mesh $\{8\,n \times 4\,n \times 1\}$ for 3 values of n.

Figure 23 shows nonlinear load curves using the regular mesh $\{8\,n \times 4\,n \times 1\}$ for different values of n. Again it can be seen that (G) predicts more flexible response than (Q1P0) for the coarser meshes. Figure 24 shows the deformed shapes for the regular mesh $\{8\,n \times 4\,n \times 1\}$ with $n = 3$ for different values of loads. In particular, it can be seen that the flexibility of (G) allows the elements near the plate's corner to roll around the corner more easily than allowed by (Q1P0). Since the flexibility of (G) has been validated relative to the mixed higher order element (HO9) it is concluded that the stiffness shown by (Q1P0) is unphysical.

4.10. *Indentation of a rigid plate into a nearly incompressible block (large deformations).* Figure 25 shows a sketch of one fourth of a nearly incompressible block that has total length $2L$, height L and depth $2L$ with

$$L = 1 \, \text{m}. \tag{4.25}$$

G   Q1P0

Figure 24. Plane strain indentation of a rigid plate into a nearly incompressible block showing the deformed shapes for the regular mesh $\{8\,n \times 4\,n \times 1\}$ with $n = 5$. The left column shows the results for (G) and the right column shows the results (Q1P0).

The bottom ($X_3^* = 0$) and exterior lateral surfaces ($X_1^* = \pm L$, $X_2^* = \pm L$) of the block remain in contact with and slide freely on smooth rigid planes. The block's top surface ($X_3^* = L$) is loaded by a rigid plate (ABCD) which makes perfect contact with the material points so that these points can only move vertically in the e_3 direction. The remaining portion of the block's top surface is traction free. Irregular elements are generated by moving the nodes of the center plane by the displacements $\{a_1, a_2, a_3, a_4\}$ as shown in Figure 25 with

$$a_1 = a, \quad a_2 = 0, \quad a_3 = -a, \quad a_4 = a, \quad -1 \leq \frac{8a}{3L} \leq 1. \tag{4.26}$$
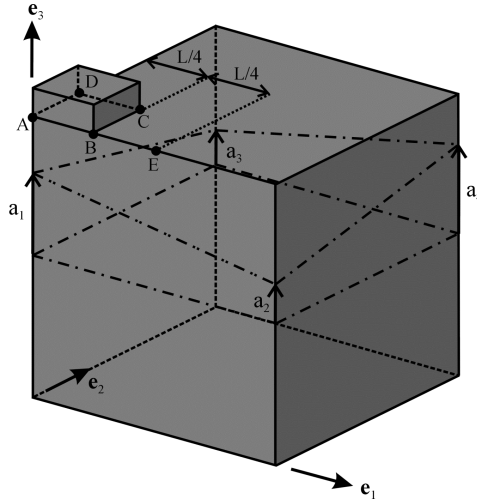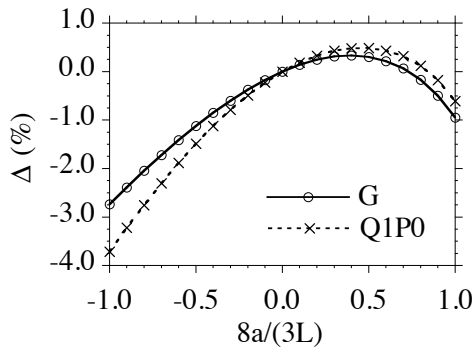
Figure 25. Indentation of a rigid plate into a block showing the boundary conditions and definition of element irregularity. Symmetry conditions are used so that only one fourth of the block is meshed.

The mesh for the one fourth region is specified by $\{4n \times 4n \times 4n\}$ with $2n$ elements below and above the distorted center surface and with $\{n \times n\}$ elements under the rigid plate. Moreover, the vertical reference locations of material points on these distorted surfaces are described by a bilinear form of the coordinates (X_1^*, X_2^*). Furthermore, the point E is located at a distance $L/4$ from the edge of the rigid plate.

Based on the results of the previous example it is expected that the deformation will be concentrated near the edges of the plate so that a refined mesh will be required to obtain an accurate solution. Mesh refinement of this 3-D problem is beyond the capacity of the hardware being used to obtain the solution. Therefore, attention will be focused on the robustness of the solutions with relative coarse meshes.

Figure 26 explores the sensitivity of the elements {G, Q1P0} to irregularity of the reference element shape. Since the converged value of the displacement u_{E3} is not known it is convenient to define the difference of u_{E3} relative to the value u_{E3}^* predicted for a regular mesh ($a = 0$). Specifically, the value

Figure 26. Indentation of a rigid plate into a nearly incompressible block. The displacement u_{E3} of the point E as a function of element irregularity for the mesh $\{4n \times 4n \times 4n\}$ with $n = 3$ and $u_{A3} = -0.1$ m.
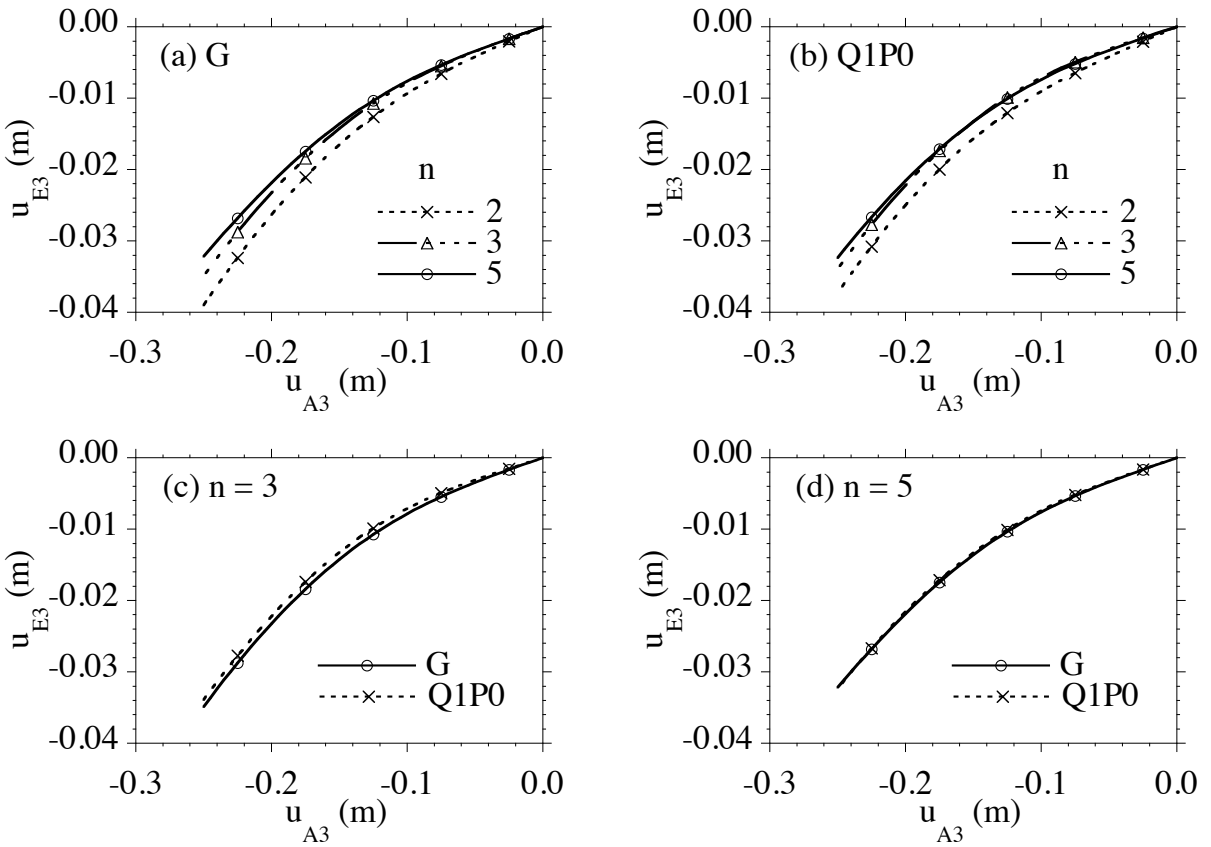
Figure 27. Indentation of a rigid plate into a nearly incompressible block. Nonlinear load curves for the regular mesh $\{4n \times 4n \times 4n\}$ with different values of n.

of u_{E3}^* for each element for the regular mesh $\{4n \times 4n \times 4n\}$ with $n = 3$ and $u_{A3} = -0.1$ m is given by

$$u_{E3}^* = -0.0078595 \text{ m} \quad \text{for } (G), \qquad u_{E3}^* = -0.0071327 \text{ m} \quad \text{for } (Q1P0). \tag{4.27}$$

The difference Δ is then defined by a formula of the type (4.7)

$$\Delta = \frac{u_{E3} - u_{E3}^*}{|u_{E3}^*|}, \tag{4.28}$$

for each of the elements using its value of u_{E3}^* so that Δ vanishes for each element when $a = 0$. The results in Figure 26 demonstrate that (G) can be used for three-dimensional irregularity of the reference element shapes and that the predictions of (G) are similar to those of (Q1P0). Since the solution is not fully converged for this mesh it is expected that the solution will be sensitive to the value of the irregularity parameter a. In particular, the results in Figure 26 are consistent with the observation that the mesh is more refined under the rigid plate for positive values of a.

Figure 27 shows nonlinear load curves using the regular mesh $\{4n \times 4n \times 4n\}$ for different values of n. From these figures it can be seen that the results predicted by $\{G, Q1P0\}$ are similar. In particular,

the unphysical stiffness exhibited by (Q1P0) in the previous plane strain problem is not detected in this three-dimensional problem.

5. Conclusions

A generalized form (2.11) for the strain energy of inhomogeneous deformations of a Cosserat point element (CPE) has been developed which includes full coupling of bending and torisonal modes. The dependence of the constitutive coefficients B_{ij} on the metric D_{ij} (3.4) have been determined by matching exact small deformation solutions for pure bending (eighteen solutions) and simple torsion (6 solutions). These coefficients are then used with nonlinear strain measures to characterize the response of general irregular element shapes to large deformations.

Ideally, for a fully converged solution the response of a structure to a specified load should be insensitive to irregularities in the element shapes used to mesh the structure. The results here indicate that the main features of this desired response for general shaped elements can be obtained by properly modeling pure bending and simple torsion of parallelepipeds with two right angles. Also, it is recalled [Jabareen and Rubin 2007b] that insensitivity to element irregularity can best be exhibited by focusing attention on a thin structure that is loaded so that inhomogeneous deformations (like bending and torsion) dominate homogeneous deformations. In particular, plots like Figure 4c for (I) clearly emphasize undesirable sensitivity to element irregularity.

In contrast with standard finite elements, the nodal forces in the generalized CPE are determined by algebraic expressions in terms of derivatives of a strain energy function and no integration is needed over the element region. A number of example problems (also see [Jabareen and Rubin 2007a; Jabareen and Rubin 2007b]) have been considered which show that the generalized CPE is as accurate as elements based on enhanced strain and incompatible modes and is as robust as elements based on full integration. The plane strain example of indentation of a rigid plate into a nearly incompressible block showed that the flexibility exhibited by the CPE is physical and that the mixed Q1P0 element predicts unphysical stiffness. Furthermore, the generalized CPE can be used to model 3-D bodies, thin shells and rods and nearly incompressible materials. In addition, the generalized CPE is free of hourglass instabilities that are observed in other element formulations in regions experiencing combined high compression with bending. Consequently, the generalized CPE is truly a robust user friendly element that can be used with confidence to model problems in nonlinear elasticity.

Appendix A. Values of the constitutive coefficients B_{ij}

The equations of the bending and torsion problems discussed in Section 3 for the element shapes can be solved for the values of B_{ij} in the strain energy function (2.11) for inhomogeneous deformations and the results were reported in [Jabareen and Rubin 2008b]. Specifically, the nonzero components of the upper diagonal of the symmetric matrices $\{B_{ij}^0, B_{ij}^{12}, B_{ij}^{13}, B_{ij}^{23}, i, j = 1, 2, \ldots, 9\}$ in (3.24) for a general shaped element are specified by

$$B_{11}^0 = 1, \qquad B_{11}^{12} = 1 + \frac{H_1^2 D_{12}^2}{H_2^2}, \qquad B_{11}^{13} = 1 + \frac{(1-\nu)\{H_1^2(1-D_{13}^2) + H_2^2\}D_{13}^2}{2H_2^2(1-D_{13}^2)}, \qquad B_{11}^{23} = 1,$$

$$B_{12}^0 = \nu, \qquad B_{12}^{12} = \nu, \qquad B_{12}^{13} = \nu - \frac{(1-\nu)D_{13}^2}{2(1-D_{13}^2)}, \qquad B_{12}^{23} = \nu, \quad B_{13}^{12} = \frac{(H_1^2 + H_2^2)D_{12}}{H_1 H_2},$$

$$B_{14}^{12} = \frac{\nu H_1 D_{12}}{H_2}, \qquad B_{16}^{23} = \frac{\nu H_2 D_{23}}{H_3}, \qquad B_{17}^{13} = \frac{(1-\nu)\{H_1^2(1-D_{13}^2) + H_2^2\}D_{13}}{2H_2 H_3(1-D_{13}^2)},$$

$$B_{18}^{13} = \frac{(1-\nu)H_1^2 D_{13}}{2H_2^2}, \qquad B_{19}^{13} = -\frac{(1-\nu)H_2 D_{13}}{2H_1(1-D_{13}^2)},$$

$$B_{22}^0 = 1, \; B_{22}^{12} = 1, \qquad B_{22}^{13} = 1 + \frac{(1-\nu)\{H_3^2(1-D_{13}^2) + H_2^2\}D_{13}^2}{2H_2^2(1-D_{13}^2)}, \qquad B_{22}^{23} = 1 + \frac{H_3^2 D_{23}^2}{H_2^2},$$

$$B_{23}^{12} = \frac{\nu H_2 D_{12}}{H_1}, \qquad B_{25}^{23} = \frac{\nu H_3 D_{23}}{H_2}, \qquad B_{26}^{23} = \frac{(H_2^2 + H_3^2)D_{23}}{H_2 H_3},$$

$$B_{27}^{13} = -\frac{(1-\nu)H_2 D_{13}}{2H_3(1-D_{13}^2)}, \qquad B_{28}^{13} = \frac{(1-\nu)H_3^2 D_{13}}{2H_2^2}, \qquad B_{29}^{13} = \frac{(1-\nu)\{H_2^2 + H_3^2(1-D_{13}^2)\}D_{13}}{2H_1 H_2(1-D_{13}^2)},$$

$$B_{33}^0 = 1, \qquad B_{33}^{12} = 1 + \frac{H_2^2 D_{12}^2}{H_1^2}, \qquad B_{33}^{13} = 1, \qquad B_{33}^{23} = 1 + \frac{(1-\nu)\{H_1^2 + H_2^2(1-D_{23}^2)\}D_{23}^2}{2H_1^2(1-D_{23}^2)},$$

$$B_{34}^0 = \nu, \qquad B_{34}^{12} = \nu, \qquad B_{34}^{13} = \nu, \qquad B_{34}^{23} = \nu - \frac{(1-\nu)D_{23}^2}{2(1-D_{23}^2)},$$

$$B_{35}^{13} = \frac{\nu H_1 D_{13}}{H_3}, \qquad B_{37}^{23} = \frac{(1-\nu)\{H_1^2 + H_2^2(1-D_{23}^2)\}D_{23}}{2H_1 H_3(1-D_{23}^2)}, \qquad B_{38}^{23} = -\frac{(1-\nu)H_1 D_{23}}{2H_2(1-D_{23}^2)},$$

$$B_{39}^{23} = \frac{(1-\nu)H_2^2 D_{23}}{2H_1^2}, \qquad B_{44}^0 = 1, \qquad B_{44}^{12} = 1, \qquad B_{44}^{13} = 1 + \frac{H_3^2 D_{13}^2}{H_1^2},$$

$$B_{44}^{23} = 1 + \frac{(1-\nu)\{H_1^2 + H_3^2(1-D_{23}^2)\}D_{23}^2}{2H_1^2(1-D_{23}^2)}, \qquad B_{45}^{13} = \frac{(H_1^2 + H_3^2)D_{13}}{H_1 H_3}, \qquad B_{46}^{13} = \frac{\nu H_3 D_{13}}{H_1},$$

$$B_{47}^{23} = -\frac{(1-\nu)H_1 D_{23}}{2H_3(1-D_{23}^2)}, \qquad B_{48}^{23} = \frac{(1-\nu)\{H_1^2 + H_3^2(1-D_{23}^2)\}D_{23}}{2H_1 H_2(1-D_{23}^2)}, \qquad B_{49}^{23} = \frac{(1-\nu)H_3^2 D_{23}}{2H_1^2},$$

$$B_{55}^0 = 1, \; B_{55}^{12} = 1 + \frac{(1-\nu)\{H_1^2(1-D_{12}^2) + H_3^2\}D_{12}^2}{2H_3^2(1-D_{12}^2)}, \qquad B_{55}^{13} = 1 + \frac{H_1^2 D_{13}^2}{H_3^2}, \qquad B_{55}^{23} = 1,$$

$$B_{56}^0 = \nu, \qquad B_{56}^{12} = \nu - \frac{(1-\nu)D_{12}^2}{2(1-D_{12}^2)}, \qquad B_{56}^{13} = \nu, \quad B_{56}^{23} = \nu,$$

$$B_{57}^{12} = \frac{(1-\nu)H_1^2 D_{12}}{2H_3^2}, \qquad B_{58}^{12} = \frac{(1-\nu)\{H_1^2(1-D_{12}^2) + H_3^2\}D_{12}}{2H_2 H_3(1-D_{12}^2)}, \qquad B_{59}^{12} = -\frac{(1-\nu)H_3 D_{12}}{2H_1(1-D_{12}^2)},$$

$$B_{66}^0 = 1, \qquad B_{66}^{12} = 1 + \frac{(1-\nu)\{H_2^2(1-D_{12}^2) + H_3^2\}D_{12}^2}{2H_3^2(1-D_{12}^2)}, \qquad B_{66}^{13} = 1, \qquad B_{66}^{23} = 1 + \frac{H_2^2 D_{23}^2}{H_3^2},$$

$$B_{67}^{12} = \frac{(1-\nu)H_2^2 D_{12}}{2H_3^2}, \qquad B_{68}^{12} = -\frac{(1-\nu)H_3 D_{12}}{2H_2(1-D_{12}^2)}, \qquad B_{69}^{12} = \frac{(1-\nu)\{H_2^2(1-D_{12}^2) + H_3^2\}D_{12}}{2H_1 H_3(1-D_{12}^2)},$$

$$B_{77}^0 = \frac{(1-\nu)(H_1^2 + H_2^2)}{2H_3^2}, \quad B_{77}^{12} = B_{77}^0, \quad B_{77}^{13} = B_{77}^0 + \frac{(1-\nu)H_2^2 D_{13}^2}{2H_3^2(1-D_{13}^2)}, \quad B_{77}^{23} = B_{77}^0 + \frac{(1-\nu)H_1^2 D_{23}^2}{2H_3^2(1-D_{23}^2)},$$

$$B_{78}^0 = \frac{(1-\nu)H_1^2}{2H_2 H_3}, \quad B_{78}^{12} = B_{78}^0, \quad B_{78}^{13} = B_{78}^0, \quad B_{78}^{23} = B_{78}^0 - \frac{(1-\nu)H_1^2 D_{23}^2}{2H_2 H_3(1-D_{23}^2)},$$

$$B_{79}^0 = \frac{(1-\nu)H_2^2}{2H_1 H_3}, \quad B_{79}^{12} = B_{79}^0, \quad B_{79}^{13} = B_{79}^0 - \frac{(1-\nu)H_2^2 D_{13}^2}{2H_1 H_3(1-D_{13}^2)}, \quad B_{79}^{23} = B_{79}^0,$$

$$B_{88}^0 = \frac{(1-\nu)(H_1^2 + H_3^2)}{2H_2^2}, \quad B_{88}^{12} = B_{88}^0 + \frac{(1-\nu)H_3^2 D_{12}^2}{2H_2^2(1-D_{12}^2)}, \quad B_{88}^{13} = B_{88}^0, \quad B_{88}^{23} = B_{88}^0 + \frac{(1-\nu)H_1^2 D_{23}^2}{2H_2^2(1-D_{23}^2)},$$

$$B_{89}^0 = \frac{(1-\nu)H_3^2}{2H_1 H_2}, \quad B_{89}^{12} = B_{89}^0 - \frac{(1-\nu)H_3^2 D_{12}^2}{2H_1 H_2(1-D_{12}^2)}, \quad B_{89}^{13} = B_{89}^0, \quad B_{89}^{23} = B_{89}^0,$$

$$B_{99}^0 = \frac{(1-\nu)(H_2^2 + H_3^2)}{2H_1^2}, \quad B_{99}^{12} = B_{99}^0 + \frac{(1-\nu)H_3^2 D_{12}^2}{2H_1^2(1-D_{12}^2)}, \quad B_{99}^{13} = B_{99}^0 + \frac{(1-\nu)H_2^2 D_{13}^2}{2H_1^2(1-D_{13}^2)}, \quad B_{99}^{23} = B_{99}^0,$$

with $\{\lambda_{12}, \lambda_{13}, \lambda_{23}\}$ defined by (3.23).

Acknowledgements

References

[ABAQUS] *ABAQUS*, Version 6.5-1, ABAQUS, Providence, RI.

[ADINA] *ADINA*, Version 8.3.1, ADINA R & D, Watertown, MA.

[ANSYS] *ANSYS*, University Advanced Version 9, ANSYS, Canonsburg, PA.

[Belytschko and Bindeman 1993] T. Belytschko and L. P. Bindeman, "Assumed strain stabilization of the eight node hexahedral element", *Comput. Methods Appl. Mech. Eng.* **105**:2 (1993), 225–260.

[Belytschko et al. 1984] T. Belytschko, J. S.-J. Ong, W. K. Liu, and J. M. Kennedy, "Hourglass control in linear and nonlinear problems", *Comput. Methods Appl. Mech. Eng.* **43**:3 (1984), 251–276.

[Boerner et al. 2007] E. F. I. Boerner, S. Loehnert, and P. Wriggers, "A new finite element based on the theory of a Cosserat point: extension to initially distorted elements for 2D plane strain", *Int. J. Numer. Methods Eng.* **71**:4 (2007), 454–472.

[Bonet and Bhargava 1995] J. Bonet and P. Bhargava, "A uniform deformation gradient hexahedron element with artificial hourglass control", *Int. J. Numer. Methods Eng.* **38**:16 (1995), 2809–2828.

[Crisfield et al. 1995] M. A. Crisfield, G. F. Moita, L. P. R. Lyons, and G. Jelenić, "Enhanced lower-order element formulations for large strains", *Comput. Mech.* **17**:1–2 (1995), 62–73.

[Ehrlich 2007] D. Ehrlich, Personal communication, 2007.

[Flory 1961] P. J. Flory, "Thermodynamic relations for high elastic materials", *T. Faraday Soc.* **57** (1961), 829–838.

[Hutter et al. 2000] R. Hutter, P. Hora, and P. Niederer, "Total hourglass control for hyperelastic materials", *Comput. Methods Appl. Mech. Eng.* **189**:3 (2000), 991–1010.

[Jabareen and Rubin 2007a] M. Jabareen and M. B. Rubin, "Hyperelasticity and physical shear buckling of a block predicted by the Cosserat point element compared with inelasticity and hourglassing predicted by other element formulations", *Comput. Mech.* **40**:3 (2007), 447–459.

[Jabareen and Rubin 2007b] M. Jabareen and M. B. Rubin, "An improved 3-D brick Cosserat point element for irregular shaped elements", *Comput. Mech.* **40**:6 (2007), 979–1004.

[Jabareen and Rubin 2008a] M. Jabareen and M. B. Rubin, "A Cosserat point element (CPE) for nearly planar problems (including thickness changes) in nonlinear elasticity", *Int. J. Eng. Sci.* **46**:10 (2008), 986–1010.

[Jabareen and Rubin 2008b] M. Jabareen and M. B. Rubin, "A generalized Cosserat point element (CPE) for isotropic nonlinear elastic materials including irregular 3-D brick and thin structures", United States Patent and Trademark Office, 2008.

[Jabareen and Rubin 2008c] M. Jabareen and M. B. Rubin, "Modified torsion coefficients for a 3-D brick Cosserat point element", *Comput. Mech.* **41**:4 (2008), 517–525.

[Loehnert et al. 2005] S. Loehnert, E. F. I. Boerner, M. B. Rubin, and P. Wriggers, "Response of a nonlinear elastic general Cosserat brick element in simulations typically exhibiting locking and hourglassing", *Comput. Mech.* **36**:4 (2005), 255–265.

[Nadler and Rubin 2003] B. Nadler and M. B. Rubin, "A new 3-D finite element for nonlinear elasticity using the theory of a Cosserat point", *Int. J. Solids Struct.* **40**:17 (2003), 4585–4614.

[Reese and Wriggers 1996] S. Reese and P. Wriggers, "Finite element calculation of the stability behaviour of hyperelastic solids with the enhanced strain methods", *Z. Angew. Math. Mech.* **76**:S5 (1996), 415–416.

[Reese and Wriggers 2000] S. Reese and P. Wriggers, "A stabilization technique to avoid hourglassing in finite elasticity", *Int. J. Numer. Methods Eng.* **48**:1 (2000), 79–109.

[Reese et al. 2000] S. Reese, P. Wriggers, and B. D. Reddy, "A new locking-free brick element technique for large deformation problems in elasticity", *Compos. Struct.* **75**:3 (2000), 291–304.

[Rubin 1995] M. B. Rubin, "Numerical solution of two- and three-dimensional thermomechanical problems using the theory of a Cosserat point", pp. 308–334 in *Theoretical, experimental, and numerical contributions to the mechanics of fluids and solids: a collection of papers in honor of Paul M. Naghdi*, edited by J. Casey and M. J. Crochet, Birkäuser, Basel, 1995. Special issue of Z. Angew. Math. Phys. **46**.

[Rubin 2000] M. B. Rubin, *Cosserat theories: shells, rods and points*, Solid Mechanics and its Applications **79**, Kluwer, Dordrecht, 2000.

[César de Sá et al. 2001] J. M. A. César de Sá, P. M. A. Areias, and R. M. N. Jorge, "Quadrilateral elements for the solution of elasto-plastic finite strain problems", *Int. J. Numer. Methods Eng.* **51**:8 (2001), 883–917.

[Simo and Armero 1992] J. C. Simo and F. Armero, "Geometrically non-linear enhanced strain mixed methods and the method of incompatible modes", *Int. J. Numer. Methods Eng.* **33**:7 (1992), 1413–1449.

[Simo and Rifai 1990] J. C. Simo and M. S. Rifai, "A class of mixed assumed strain methods and the method of incompatible modes", *Int. J. Numer. Methods Eng.* **29**:8 (1990), 1595–1638.

[Simo et al. 1993] J. C. Simo, F. Armero, and R. L. Taylor, "Improved versions of assumed enhanced strain tri-linear elements for 3D finite deformation problems", *Comput. Methods Appl. Mech. Eng.* **110**:3–4 (1993), 359–386.

[Sokolnikoff 1956] I. S. Sokolnikoff, *Mathematical theory of elasticity*, McGraw-Hill, New York, 1956.

[Taylor 2005] R. L. Taylor, "FEAP - a finite element analysis program, Version 7.5", University of California, Berkeley, 2005.

[Zienkiewicz and Taylor 2005] O. C. Zienkiewicz and R. L. Taylor, *The finite element method for solid and structural mechanics*, 6th ed., Elsevier, Amsterdam, 2005.

M. JABAREEN: mahmood.jabareen@imes.mavt.ethz.ch
Institute of Mechanical Systems, Department of Mechanical Engineering, ETH Zentrum, 8092 Zürich, Switzerland

M. B. RUBIN: mbrubin@tx.technion.ac.il
Faculty of Mechanical Engineering, Technion – Israel Institute of Technology, 32000 Haifa, Israel